

**CO<sub>2</sub> flux history  
1982–2001**

C. Rödenbeck et al.

# CO<sub>2</sub> flux history 1982–2001 inferred from atmospheric data using a global inversion of atmospheric transport

C. Rödenbeck<sup>1</sup>, S. Houweling<sup>2</sup>, M. Gloor<sup>1</sup>, and M. Heimann<sup>1</sup>

<sup>1</sup>Max Planck Institute for Biogeochemistry, Postfach 10 01 64, D-07701 Jena, Germany

<sup>2</sup>National Institute for Space Research (SRON), Princetonplein 5, NL-3584 CC Utrecht, The Netherlands

Received: 14 March 2003 – Accepted: 1 May 2003 – Published: 19 May 2003

Correspondence to: C. Rödenbeck (christian.roedenbeck@bgc-jena.mpg.de)

[Title Page](#)

[Abstract](#)

[Introduction](#)

[Conclusions](#)

[References](#)

[Tables](#)

[Figures](#)

[I◀](#)

[▶I](#)

[◀](#)

[▶](#)

[Back](#)

[Close](#)

[Full Screen / Esc](#)

[Print Version](#)

[Interactive Discussion](#)

© EGU 2003

## Abstract

Based on about 20 years of NOAA/CMDL's atmospheric CO<sub>2</sub> concentration data and a global atmospheric tracer transport model, we estimate interannual variations and spatial patterns of surface CO<sub>2</sub> fluxes in the period 01/1982–12/2000, by using a time-dependent Bayesian inversion technique. To increase the reliability of the estimated temporal features, particular care is exerted towards the selection of data records that are homogeneous in time. Fluxes are estimated on a grid-scale resolution ( $\approx 8^\circ$  latitude  $\times 10^\circ$  longitude), constrained by a-priori spatial correlations, and then integrated over different sets of regions. The transport model is driven by interannually varying re-analysed meteorological fields. We make consistent use of unsmoothed measurements. In agreement with previous studies, land fluxes are estimated to be the main driver of interannual variations in the global CO<sub>2</sub> fluxes, with the pace predominantly being set by the El Niño/La Niña contrast. An exception is a 2–3 year period of increased sink of atmospheric carbon after Mt. Pinatubo's volcanic eruption in 1991. The largest differences in fluxes between El Niño and La Niña are found in the tropical land regions, the main share being due to the Amazon basin. The flux variations for the Post-Pinatubo period, the 1997/1998 El Niño, and the 1999 La Niña events are exploited to investigate relations between CO<sub>2</sub> fluxes and climate forcing. A rough comparison points to anomalies in precipitation as a prominent climate factor for short-term variability of tropical land fluxes, both through their role on NPP and through promoting fire in case of droughts. Some large flux anomalies seem to be directly related to large biomass burning events recorded by satellite observation. Global ocean carbon uptake shows a trend similar to the one expected if ocean uptake scales proportional to the anthropogenic atmospheric perturbation. In contrast to temporal variations, the longterm spatial flux distribution can be inferred with lesser robustness only. The tentative pattern estimated by the present inversion exhibits a northern hemisphere land sink on the order of 0.4 PgC/yr (for 01/1996–12/1999, non-fossil fuel carbon only) that is mainly confined to North America. Southern hemisphere land regions are carbon neu-

## CO<sub>2</sub> flux history 1982–2001

C. Rödenbeck et al.

Title Page

Abstract

Introduction

Conclusions

References

Tables

Figures

◀

▶

◀

▶

Back

Close

Full Screen / Esc

Print Version

Interactive Discussion

tral, while the tropical land regions are taking up carbon (e.g., at a rate of 0.8 PgC/yr during 01/1996–12/1999). Ocean fluxes show larger uptake in the Northern mid to high latitudes than in the Southern mid latitude regions, in contrast to the estimates by Takahashi et al. (1999) based on in-situ measurements. On a regional basis, results that differ the most from previous estimates are large carbon uptake of 1 to 1.5 PgC/yr by the Southern temperate Pacific ocean region, weak outgassing from the Southern ocean, and a carbon source from eastern Europe.

## 1. Introduction

Many lines of evidence indicate that the observed rise of the atmospheric CO<sub>2</sub> concentration since preindustrial times is caused by anthropogenic CO<sub>2</sub> emissions from fossil fuel burning, cement manufacturing, and land use change such as deforestation. However, the actual atmospheric CO<sub>2</sub> increase is significantly modified by ocean uptake and exchange fluxes with the terrestrial biosphere: This is already strongly indicated by the observations that the increase of the total atmospheric CO<sub>2</sub> content corresponds only to roughly one third of the anthropogenic emissions, and shows both a pronounced seasonality (Bolin and Keeling, 1963) and inter-annual variations reminiscent of vegetation responses to climatic variations (Keeling et al., 1995; Francey et al., 1995). Future projection of the global climate, therefore, requires quantitative understanding of the role of ocean and land biosphere in the global carbon budget, in particular their response and feedback to climatic controls. On a leaf, plant, or ecosystem level, much understanding has been achieved by process studies (e.g. Schulze, 2000; Barford et al., 2001; Falge et al., 2002). It remains difficult, however, to extrapolate these results to regional or continental scales. A possibility to gain information on short-term responses of ecosystems on large spatial scales is to relate the interannual variations of surface exchange fluxes to the observed variations of potential underlying drivers. As an example, correlations between short-term land flux anomalies and the anomaly patterns in variables such as temperature, precipitation, or light availability in-

Title Page

Abstract

Introduction

Conclusions

References

Tables

Figures

◀

▶

◀

▶

Back

Close

Full Screen / Esc

Print Version

Interactive Discussion

**CO<sub>2</sub> flux history  
1982–2001**

C. Rödenbeck et al.

Title Page

Abstract

Introduction

Conclusions

References

Tables

Figures

◀

▶

◀

▶

Back

Close

Full Screen / Esc

Print Version

Interactive Discussion

© EGU 2003

dicating that the biosphere reacts in some coherent way to the respective climatic driver (strong natural modes of variability – in particular the El Niño/La Niña cycle and the transient consequences of the Mt. Pinatubo volcanic eruption – are exploited here as the ‘laboratory assistant’ that varies the control parameters for us).

This approach requires to quantify the history of land-atmosphere and ocean-atmosphere carbon fluxes. While it is not possible to directly and comprehensively measure all CO<sub>2</sub> fluxes emitted or taken up by the different parts of the globe, we have an unbribable witness of this entire flux history: the atmosphere itself. Its evidence has been recorded at a network of stations regularly measuring CO<sub>2</sub> concentrations (one of the first stations, at Mauna Loa (Hawaii), started measuring in 1958). To unravel the information on surface sources and sinks contained in these data, an atmospheric transport model may be used in an inverse mode: Given the temporal and spatial patterns of the concentrations, the inverse technique allows to estimate plausible temporal and spatial patterns of surface fluxes, by minimizing the mismatch between measured and modelled concentrations. Atmospheric inversions have a long tradition in which more and more modes of flux variability (spatial patterns, the seasonal cycle, inter-annual variations) that have previously been prescribed, are now explicitly estimated. Estimates of interannual CO<sub>2</sub> fluxes were first performed by Rayner et al. (1999). The technique was further developed e.g. by Bousquet et al. (2000). We extend here the method to overcome a number of problems: (1) avoiding spurious variability by selection of homogeneous data records, (2) avoiding ‘spatial rectification biases’ by solving for highly-resolved fluxes correlated in space and time (Houweling et al., in preparation), (3) reduction of model representation errors by use of interannually varying meteorological drivers and consistent representation of data sampling in the model (Rödenbeck et al., 2003). The estimates are based on CO<sub>2</sub> concentration data from the years 1980 through 2001 measured by NOAA/CMDL (update of Conway et al., 1994). This study thus provides an updated estimate of the CO<sub>2</sub> flux history.

Section 2 is devoted to the inversion method, explaining its concept and specifying the particular set-up and input data that were used in the present study. In Sect. 3,

Title Page

Abstract

Introduction

Conclusions

References

Tables

Figures

◀

▶

◀

▶

Back

Close

Full Screen / Esc

Print Version

Interactive Discussion

© EGU 2003

the resulting CO<sub>2</sub> flux estimates are presented and described on several different spatial and temporal scales. As a prerequisite for any interpretation, Sect. 4 explores the degree of robustness of different aspects of these estimates, identifying the sufficiently credible features. Time averaged spatial patterns are discussed in Sect. 5, while Sect. 6 discusses the implications of temporal patterns found in the flux estimates with special emphasis on potential drivers of the estimated CO<sub>2</sub> fluxes.

## 2. Inversion Method

### 2.1. Concept

The inversion technique is used to estimate CO<sub>2</sub> fluxes from the combination of several distinct sources of information.

The primary source of information is measured atmospheric CO<sub>2</sub> concentrations at a set of stations. The values at different locations and different times are summarizingly denoted by the vector  $\mathbf{c}_{\text{meas}}$ .

To link these measured atmospheric concentrations to the desired surface exchange fluxes, information about the atmospheric tracer transport is required. It is obtained from simulations with a global three-dimensional transport model driven by meteorological data from a global weather prediction center. Since transport is linear, we can write the action of the tracer model as a transport matrix  $\mathbf{A}$ : For a given flux input  $\mathbf{f}$  (vector of the flux values at all grid points and time steps of the model) and a given initial concentration  $c_0$  at the beginning of the simulation period, the modelled concentration vector  $\mathbf{c}_{\text{mod}}$  is

$$\mathbf{c}_{\text{mod}} = \mathbf{A}\mathbf{f} + \mathbf{a}c_0 \quad (1)$$

where  $\mathbf{A}$  plays the role of a discrete Green's function kernel<sup>1</sup>. All elements of the vector  $\mathbf{a}$  equal 1, corresponding to an assumed initially well-mixed atmosphere.

<sup>1</sup> Each matrix element of  $\mathbf{A}$  gives the sensitivity (“concentration response”)  $\partial c_{st} / \partial f_{ijt}$  at

Theoretically, one could now find estimates of the fluxes  $\mathbf{f}$  (and the initial condition  $c_0$ ): The mismatch  $\delta\mathbf{c}$  between measured and modelled concentrations is identified with the sum of measurement errors  $\Delta\mathbf{c}_{\text{meas}}$  and model representation errors  $\Delta\mathbf{c}_{\text{mod}}$ ,

$$\begin{aligned}\delta\mathbf{c} &= \mathbf{c}_{\text{meas}} - \mathbf{c}_{\text{mod}} \\ &= \Delta\mathbf{c}_{\text{meas}} + \Delta\mathbf{c}_{\text{mod}}\end{aligned}\quad (2)$$

Model representation errors  $\Delta\mathbf{c}_{\text{mod}}$  arise because the tracer model will not be able to reproduce the true concentration field, even if a perfect flux field  $\mathbf{f}$  could be supplied. All errors are assumed to have a Gaussian probability distribution, with zero mean (i.e. unbiased) and a given covariance matrix

$$\begin{aligned}\mathbf{Q}_{\mathbf{c}} &= \langle \delta\mathbf{c}\delta\mathbf{c}^T \rangle \\ &= \langle \Delta\mathbf{c}_{\text{meas}}\Delta\mathbf{c}_{\text{meas}}^T \rangle + \langle \Delta\mathbf{c}_{\text{mod}}\Delta\mathbf{c}_{\text{mod}}^T \rangle\end{aligned}\quad (3)$$

that quantifies their magnitude ( $\Delta\mathbf{c}_{\text{meas}}$  and  $\Delta\mathbf{c}_{\text{mod}}$  are assumed uncorrelated). Then, one obtains the most probable fluxes by minimizing the cost function

$$\chi_{\mathbf{c}}^2 = \delta\mathbf{c}^T \mathbf{Q}_{\mathbf{c}}^{-1} \delta\mathbf{c}\quad (4)$$

(Gauss, 1801). The covariance matrix  $\mathbf{Q}_{\mathbf{c}}$  introduces a weighting among the concentration values which ensures that those with the smallest measurement and/or model representation errors have the largest impact on the result.

However, the available spatial coverage of concentration data would not sufficiently constrain such flux estimates, i.e. quite different flux patterns would lead to almost the same value of  $\chi_{\mathbf{c}}^2$  (Kaminski and Heimann, 2001). Within the Bayesian framework, this can partially be remedied by taking into account so-called a-priori information about the fluxes from other sources of information, such as independent measurements, model simulations, or process understanding. In contrast to the case above where any flux

some station  $s$  at some time  $t$  resulting from a unit tracer pulse emitted from some surface grid cell  $(i, j)$  at some (other) time  $t'$ .

Title Page

Abstract

Introduction

Conclusions

References

Tables

Figures

◀

▶

◀

▶

Back

Close

Full Screen / Esc

Print Version

Interactive Discussion

---

**CO<sub>2</sub> flux history  
1982–2001**

 C. Rödenbeck et al.
 

---

[Title Page](#)
[Abstract](#)
[Introduction](#)
[Conclusions](#)
[References](#)
[Tables](#)
[Figures](#)
[◀](#)
[▶](#)
[◀](#)
[▶](#)
[Back](#)
[Close](#)
[Full Screen / Esc](#)
[Print Version](#)
[Interactive Discussion](#)

© EGU 2003

value has the same a-priori probability, the a-priori probability distribution of the fluxes is now specified as a Gaussian around the best-guess values  $\mathbf{f}_{\text{pri}}$  to be specified later. The deviations from  $\mathbf{f}_{\text{pri}}$  are further structured by introducing a simple linear flux model of the form

$$\mathbf{f} = \mathbf{f}_{\text{pri}} + \mathbf{F}\delta\mathbf{s} \quad (5)$$

The flux model decomposes the deviations around  $\mathbf{f}_{\text{pri}}$  into a set of tracer pulses (tracer emissions from certain areas during certain time intervals). The elements of the vector  $\delta\mathbf{s}$  are the relative source strengths (or relative sink strengths, respectively, if negative) of these pulses, and the corresponding columns of the matrix  $\mathbf{F}$  describe their spatio-temporal form to be specified later. The parameters to be adjusted by the inversion are now the source strengths  $\delta\mathbf{s}$  rather than all the elements of  $\mathbf{f}$ . The flux model thus reduces the number of degrees of freedom of the inversion. It structures the covariance matrix of the fluxes, according to the relation

$$\mathbf{Q}_f = \mathbf{F}\mathbf{Q}_s\mathbf{F}^T \quad (6)$$

where  $\mathbf{Q}_s$  is the covariance matrix of the source strengths. This means that the spatial and temporal scales of coherent behaviour of the inversion are determined by the extension of the pulses in space and time (as described by  $\mathbf{F}$ ) as well as by any correlations among the source strengths (off-diagonal elements in  $\mathbf{Q}_s$ ). Therefore, the specification of  $\mathbf{F}$  and  $\mathbf{Q}_s$  below reflects assumptions on the processes responsible for the fluxes being estimated.

Now, the combination of transport and flux models gives

$$\mathbf{c}_{\text{mod}} = (\mathbf{A}\mathbf{f}_{\text{pri}} + \mathbf{a}c_{0,\text{pri}}) + \mathbf{M}\delta\mathbf{x} \quad (7)$$

with the extended model matrix

$$\mathbf{M} = (\mathbf{A}\mathbf{F}, \mathbf{a}) \quad (8)$$

and the extended parameter vector

$$\delta \mathbf{x} = \begin{pmatrix} \delta \mathbf{s} \\ \delta c_0 \end{pmatrix} \quad (9)$$

whose covariance matrix is

$$\mathbf{Q}_x = \begin{pmatrix} \mathbf{Q}_s & 0 \\ 0 & \sigma_{c_0}^2 \end{pmatrix} \quad (10)$$

5 To include the a-priori information, the cost function is modified to (Tarantola, 1987)

$$\chi^2 = \delta \mathbf{c}^T \mathbf{Q}_c^{-1} \delta \mathbf{c} + \delta \mathbf{x}^T \mathbf{Q}_{x,\text{pri}}^{-1} \delta \mathbf{x} \quad (11)$$

This cost function is minimal at the parameter values

$$\delta \mathbf{x}_{\text{post}} = (\mathbf{M}^T \mathbf{Q}_c^{-1} \mathbf{M} + \mathbf{Q}_{x,\text{pri}}^{-1})^{-1} \mathbf{M}^T \mathbf{Q}_c^{-1} \\ \times (\mathbf{c}_{\text{meas}} - \mathbf{A} \mathbf{f}_{\text{pri}} - \mathbf{a} c_{0,\text{pri}}) \quad (12)$$

10 The matrix inverses are solved by singular value decomposition<sup>2</sup>. Then, the flux estimates ('a-posteriori fluxes') are calculated by inserting the source strengths contained

<sup>2</sup> The matrix  $\tilde{\mathbf{M}} = \mathbf{Q}_c^{-1/2} \mathbf{M} \mathbf{Q}_{x,\text{pri}}^{1/2}$  is decomposed by SVD into a matrix product

$$\tilde{\mathbf{M}} = \mathbf{U} [\lambda] \mathbf{V}^T$$

with  $\mathbf{U}^T \mathbf{U} = \mathbf{1}$ ,  $\mathbf{V}^T \mathbf{V} = \mathbf{1}$ ,  $\mathbf{V} \mathbf{V}^T = \mathbf{1}$ , and a diagonal matrix  $[\lambda]$  of the singular values (Press et al., 1992). Then, Equation (12) becomes

$$\delta \mathbf{x}_{\text{post}} = \mathbf{Q}_{x,\text{pri}}^{1/2} \mathbf{V} [\lambda / (\lambda^2 + 1)] \mathbf{U}^T \mathbf{Q}_c^{-1/2} \\ \times (\mathbf{c}_{\text{meas}} - \mathbf{A} \mathbf{f}_{\text{pri}} - \mathbf{a} c_{0,\text{pri}})$$

In the present case, the number of parameters and therefore the number of singular vectors is large. In order to speed up the calculation, a short tail (approx. 14%) of the set of singular vectors is omitted from the matrix multiplications. The corresponding singular values are so small that they do not appreciably change the result.

[Title Page](#)
[Abstract](#)
[Introduction](#)
[Conclusions](#)
[References](#)
[Tables](#)
[Figures](#)
[◀](#)
[▶](#)
[◀](#)
[▶](#)
[Back](#)
[Close](#)
[Full Screen / Esc](#)
[Print Version](#)
[Interactive Discussion](#)



in  $\delta \mathbf{x}_{\text{post}}$  into the flux model, Eq. (5).

## 2.2. Specification of the inversion set-up

### 2.2.1. CO<sub>2</sub> concentration data

The present study is based on flask data of NOAA/CMDL's station network (update of Conway et al., 1994). For station codes, names, and locations see Table 1 and Fig. 1. Figure 2 (left part) indicates the number of measurements per month. As can be seen, the number of active stations has continuously increased during our period of interest (1982/01-2000/12) by roughly a factor of 4. Unlike previous inversion studies, only those parts of the data records that are homogeneous in time are used, allowing data gaps no longer than two months duration (a few exceptions were made, mainly for PSA, SEY, and TDF to be able to retain these important sampling locations, see Fig. 2). As demonstrated in Sect. 3, this requirement avoids spurious trends introduced otherwise by the changes in the station network in time. In order to exploit nevertheless as much data as possible, 5 different inversion runs are performed, with successively larger station sets but correspondingly shorter target periods<sup>3</sup> (Table 2). The concentration data of the individual measurements are used directly, i.e. without any previous curve-fitting, smoothing, or gap-filling (Rödenbeck et al., 2003). Values flagged by NOAA/CMDL as invalid (hard flag) were omitted from the records. Measurements (typically one pair of flasks per week, Fig. 2) are then averaged into monthly values, which form the elements of the measurement vector  $\mathbf{c}_{\text{meas}}$ . A very small number of monthly values is

<sup>3</sup> The periods of the inversion calculations are actually longer than the target periods presented as valid results. An initial 2 years spin-up period is applied to ensure a consistent three-dimensional implied initial concentration field. Likewise, the final year of the calculations is discarded as well to ensure that every flux value is constrained by at least 1 year of measurements. It was tested explicitly that the presented time span is not appreciably influenced by edge effects.

Title Page

Abstract

Introduction

Conclusions

References

Tables

Figures

◀

▶

◀

▶

Back

Close

Full Screen / Esc

Print Version

Interactive Discussion

discarded as 'obvious outliers' based on manual judgement<sup>4</sup>.

The use of data from only one measurement institution limits the maximal number of available stations. However, it ensures maximal consistency among the measurements. NOAA/CMDL publically provides unfiltered observational data which are necessary for the approach chosen here. It should also be kept in mind that, in view of record homogeneity, stations that came into operation only during recent years could not be included in the runs with the longer target periods anyway, notwithstanding their high value for future inversions.

### 2.2.2. Atmospheric transport

The transport matrix **A** is calculated by the global off-line atmospheric transport model TM3 (Heimann, 1996) with a spatial resolution of approximately 4° latitude × 5° longitude × 19 vertical levels. The model is driven by meteorological fields derived from the NCEP reanalysis (Kalnay et al., 1996) that covers all our target period in a consistent manner. The meteorological input varies interannually according to the true year of simulation (Rödenbeck et al., 2003). Concentration values are picked from the model grid box next to the station location. Modelled monthly mean concentrations are calculated by averaging over 'samples' that represent the concentrations at the same time instants as the real flask measurements were taken (Rödenbeck et al., 2003). To calculate the matrix **A** in a computationally efficient way, an 'adjoint' of the transport model (generated with the help of the TAMC software, Giering and Kaminski, 1998) was used<sup>5</sup>.

<sup>4</sup> Values are considered 'obvious outliers' if their difference from the mean seasonal cycle is comparable with the seasonal cycle amplitude and if they cause an unusually large flux deviation in a single month. If, however, the concentrations modelled from the a-priori fluxes show an anomaly of similar kind, the event is considered transport-related and retained. The judgement of 'obvious outliers' often coincides with NOAA/CMDL's soft flags, but softly flagged values are much more frequent, and most of them are considered valid here.

<sup>5</sup> Due to the high number of elements in **f** (containing fluxes at the spatial resolution of the

Title Page

Abstract

Introduction

Conclusions

References

Tables

Figures

◀

▶

◀

▶

Back

Close

Full Screen / Esc

Print Version

Interactive Discussion

### 2.2.3. Concentration uncertainty

As stated in Eq. (3), the concentration uncertainty is a quadratic sum of measurement uncertainty and model uncertainty.

The  $\pm 1\sigma$  intervals of the measured monthly mean concentrations were set to  $0.4\text{ppm}/\sqrt{n}$  (based on maximally allowed flask pair difference of 0.5 ppm (Conway et al., 1994) and intercomparison differences of 0.2 ppm (Masarie et al., 2001)) where  $n$  is the number of data values (single flasks) per month (with a maximum cut-off at  $n = 8$ ). Any error correlations are neglected.

As a proxy of the model representation error,  $\pm 1\sigma$  intervals were related to spatial and temporal gradients at the location of the individual stations<sup>6</sup>. Though merely being a rough proxy, this procedure attempts to take into account that, given the finite resolution of the model grid, the concentration field at any particular station is the less accurately represented the more heterogeneous its environment is. This generally leads to higher uncertainties for continental stations, which, in addition, are expected to be particularly affected by other errors, such as the hard-to-model vertical mixing processes. Any error correlations are neglected.

model), the row-wise calculation by the adjoint is more efficient than the column-wise calculation by the forward model.

The sensitivities of the monthly concentrations to the monthly fluxes up to 3 years back in time were explicitly calculated by the adjoint transport model. The preceding period was approximated by exponential decay (time constant: 3.5 years) towards uniform sensitivity.

<sup>6</sup> Values were obtained from a forward model run based on the a-priori fluxes. For each station, we formed time series of the standard deviations of the 16 concentration values simulated at every 2 consecutive model time steps (40 min) for the 8 grid boxes that surround the station location. The representation error was then taken as the daytime mean of these standard deviations, calculated separately for each of the 12 month of the seasonal cycle (i.e. the representation error varies seasonally, but not interannually). To respect the fact that the inversion assumes unbiased random errors while part of the unrealism of the model is certainly systematic, we did not divide by  $\sqrt{n}$  as in the case of the measurement uncertainty.

Title Page

Abstract

Introduction

Conclusions

References

Tables

Figures

◀

▶

◀

▶

Back

Close

Full Screen / Esc

Print Version

Interactive Discussion

[Title Page](#)[Abstract](#)[Introduction](#)[Conclusions](#)[References](#)[Tables](#)[Figures](#)[◀](#)[▶](#)[◀](#)[▶](#)[Back](#)[Close](#)[Full Screen / Esc](#)[Print Version](#)[Interactive Discussion](#)

© EGU 2003

The resulting ranges of total concentration uncertainties for each station are given in the right part of Fig. 2.

#### 2.2.4. A-priori information

In the flux model, three processes are taken into account:

- Anthropogenic emissions from fossil fuel burning and cement manufacturing,
- net ecosystem exchange (NEE) of the terrestrial biosphere, and
- ocean-atmosphere carbon exchange.

Correspondingly, the flux model (Eq. 5) consists of three parts,

$$\begin{aligned} \mathbf{f} = & \mathbf{f}_{\text{pri,ff}} \\ & + \mathbf{f}_{\text{pri,nee}} + \mathbf{F}_{\text{nee}} \delta \mathbf{s}_{\text{nee}} \\ & + \mathbf{f}_{\text{pri,oc}} + \mathbf{F}_{\text{oc}} \delta \mathbf{s}_{\text{oc}} \end{aligned} \quad (13)$$

where each part (i.e. each line) consists of an a-priori best-guess term, and (except for fossil fuel, see below) a deviation term involving some sub-set of the tracer pulses.

The choices for the three components of the best-guess a-priori flux,  $\mathbf{f}_{\text{pri}} = \mathbf{f}_{\text{pri,ff}} + \mathbf{f}_{\text{pri,nee}} + \mathbf{f}_{\text{pri,oc}}$ , are listed in Table 3. Except for the rising fossil fuel component,  $\mathbf{f}_{\text{pri}}$  has no year-to-year variability, in order that the interannual variability of the resulting flux estimates be dominated by that of the atmospheric concentration signal.

All columns of  $\mathbf{F}_{\text{nee}}$ , describing the tracer pulses associated with NEE, are set elementwise proportional to a fixed spatio-temporal pattern (shape)  $\mathbf{f}_{\text{sh,nee}}$ ,

$$\mathbf{F}_{\text{nee}} = [\mathbf{f}_{\text{sh,nee}}] \mathbf{G}_{\text{nee}} \quad (14)$$

(the square brackets denote the diagonal matrix formed out of the argument vector). The columns of  $\mathbf{G}_{\text{nee}}$ , with values between 0 and 1, determine the spatio-temporal extent of the individual land pulses, to be defined below. The fixed pattern  $\mathbf{f}_{\text{sh,nee}}$  is

---

**CO<sub>2</sub> flux history  
1982–2001**

C. Rödenbeck et al.

---

 Title Page

Abstract

Introduction

Conclusions

References

Tables

Figures

Back

Close

Full Screen / Esc

Print Version

Interactive Discussion

© EGU 2003

taken constant in time and proportional to annual net primary productivity (NPP) as shown in Fig. 3 (see Table 3), in order that the inversion preferentially adjusts fluxes in areas with high vegetation activity (as opposed, e.g. to deserts)<sup>7</sup>. The corresponding matrix  $\mathbf{F}_{oc}$  for the ocean pulses involves a shape  $\mathbf{f}_{sh,oc}$  which is constant in time and flat in space (i.e. proportional to water area). To avoid errors in the land/ocean partitioning arising at coastal grid cells, land and ocean shapes partially overlap, such that mixed land/water pixels are proportionally assigned to both a land and an ocean tracer pulse.

The covariance matrix  $\mathbf{Q}_s$  is, corresponding to the flux pulses, also partitioned into land and ocean contributions. Setting the diagonal elements (i.e. the variances) within each part to an equal value, would ensure that the spatial and temporal distribution of the flux uncertainties is proportional to  $\mathbf{f}_{sh,nee}$  or  $\mathbf{f}_{sh,oc}$ , respectively, both within and between the areas/durations of the tracer pulses. Together with the off-diagonal elements of  $\mathbf{Q}_s$  (i.e. the covariances) defined below, both parts are scaled by one factor each, such that the variances of the globally integrated deviation terms match the global process uncertainties of NEE (0.85 PgC/yr with respect to a 10 year average, i.e.  $\sqrt{10} \cdot 0.85$  PgC/yr for a yearly flux in the absence of time correlations) and ocean exchange (0.5 PgC/yr with respect to a 4 year average) as given in Table 3.

Ideally, we would like the inversion to partition the deviations from the a-priori fluxes among all three processes. Land and ocean fluxes can, since they are geographically separated, readily be accounted for in statistically independent deviation terms. However, the inversion cannot be expected to distinguish between land biosphere fluxes and fossil fuel emissions, because both are inextricably localized on land, and the CO<sub>2</sub> data alone do not discern fossil and non-fossil carbon. Of these two land components, the focus of this study is the biospheric fluxes, with fossil fuel emissions considered to be known much better a-priori. Therefore, the fossil fuel deviations are neglected in the flux model, taking into the bargain that any errors of the a-priori fossil fuel flux  $\mathbf{f}_{pri,ff}$  will appear as corrections to the NEE flux. To partially account for this, the a-priori flux uncertainties are artificially increased by an amount corresponding to the missing

<sup>7</sup> In sensitivity set-up (c), a flat land shape  $\mathbf{f}_{sh,nee}$  (i.e. proportional to land area) is used.

fossil fuel deviation term (assumed to have  $f_{sh,ff} = f_{pri,ff}$ ). This is done by adding a corresponding contribution to  $Q_s$ .

To finally construct the columns of  $G$  and the off-diagonal elements of  $Q_{s,pri}$ , the tracer pulses in the flux model need to be defined. Traditionally, the earth surface is divided into a set of regions (typically 22 to 80), and the time axis into monthly intervals; the pulses emitted from any such region in any month are considered independent<sup>8</sup>. In the standard set-up used here, the monthly time step is kept, but the earth surface is tiled into a regular grid of boxes (approximately 8° latitude × 10° longitude, resulting in 730 regions). This step from large regions to grid boxes is an analogue to the step from estimating yearly fluxes with a pre-assumed seasonal cycle to estimating monthly fluxes: As the explicit resolution of the seasonal cycle avoids the seasonal rectification bias (Peylin et al., 2002), the high spatial resolution avoids a corresponding bias (Kaminski et al., 2001) that could be called ‘spatial rectification bias’.

That the resulting large number of parameters in  $\delta s$  is highly underconstrained by the inversion is compensated by introducing correlations among them. Exponentially decaying spatial correlations with a length scale of 1275 km (NEE), 1912 km (ocean), or 6375 km (fossil fuel) were chosen (corresponding to 0.2, 0.3, or 1 Earth radii)<sup>9</sup>; there is no cross-correlation assumed between land and ocean fluxes. More details can be

<sup>8</sup> In sensitivity set-up (b), such a region definition with independent pulses from 39 regions is used.

<sup>9</sup> The chosen spatial scales of correlation are based on statistical analyses of the results of the model intercomparisons CCMLP [terrestrial biosphere] and OCMIP-2 [oceans], respectively. An exponential decay function was fitted to the sum of all individual auto-correlation functions and all cross-correlation functions of the respective group of models. The resulting average spatial scale at which the models are correlated is taken as a proxy of the correlation length of our prior uncertainties. This assumes that ranges of model results reflect real uncertainties. This is unlikely to be true, but considered a reasonable first order approximation lacking a more appropriate measure.

Title Page

Abstract

Introduction

Conclusions

References

Tables

Figures

◀

▶

◀

▶

Back

Close

Full Screen / Esc

Print Version

Interactive Discussion

Title Page

Abstract

Introduction

Conclusions

References

Tables

Figures

◀

▶

◀

▶

Back

Close

Full Screen / Esc

Print Version

Interactive Discussion

© EGU 2003

found in Houweling et al. (in preparation)<sup>10</sup>. These spatial correlations are implemented by corresponding off-diagonal elements in the parameter covariance matrix  $\mathbf{Q}_s$  (cmp. Eq. (6)). In time, no correlations are applied in the standard set-up<sup>11</sup>.

### 2.3. Quantification of errors in the estimates

In addition to the estimated fluxes, a quantitative measure of their uncertainty is needed. On the one hand, formal error propagation provides  $\pm 1\sigma$  intervals (and correlations) of the result, contained in the a-posteriori covariance matrix  $\mathbf{Q}_{f,\text{post}}$ . It is obtained via Eq. (6) from the a-posteriori covariance matrix of the parameters,

$$\mathbf{Q}_{\mathbf{x},\text{post}} = (\mathbf{M}^T \mathbf{Q}_c^{-1} \mathbf{M} + \mathbf{Q}_{\mathbf{x},\text{pri}}^{-1})^{-1}. \quad (15)$$

Thus, the specified a-priori uncertainties  $\mathbf{Q}_c$  and  $\mathbf{Q}_{\mathbf{x},\text{pri}}$  serve two purposes: weighting among the input items in the cost function Eq. (11), and giving a-posteriori uncertainties. The a-posteriori error is necessarily smaller than the a-priori error, reflecting the information of the concentration data that has been added (Tarantola, 1987).

The a-posteriori uncertainties in  $\mathbf{Q}_{f,\text{post}}$  describe random errors that the inversion result inherits from the random errors of the input quantities, being quantified a-priori by  $\mathbf{Q}_c$  and  $\mathbf{Q}_{\mathbf{x},\text{pri}}$ . However, since this quantification is mainly based on proxy information, the actual error distribution is expected to be only broadly captured. As a consequence, the inversion directs the flux adjustments necessary to fit the data towards those locations/periods where the largest uncertainties have been specified, not necessarily

<sup>10</sup> Viewed in terms of such correlations, the large-region approach corresponds to perfect correlation within the individual large regions, i.e. the implied correlation length is then set by the region size (Sect. 2.1).

<sup>11</sup> In sensitivity set-up (d), fluxes are correlated on a 2 months scale, by changing the columns of  $\mathbf{G}$  from disjunct pulses with rectangular time course (on/off) to pulses with a triangular time course (linearly increasing/decreasing) overlapping their neighbours over 2 months. By Eq. (6), this leads to Gaussian-like correlations (with complete decay already after 4 months) in the fluxes.

**CO<sub>2</sub> flux history  
1982–2001**

C. Rödenbeck et al.

Title Page

Abstract

Introduction

Conclusions

References

Tables

Figures

◀

▶

◀

▶

Back

Close

Full Screen / Esc

Print Version

Interactive Discussion

© EGU 2003

where the a-priori fluxes are most unrealistic. This is also true for the coherency over certain areas/intervals (as specified by the a-priori correlation structure). Also, e.g. the model representation errors can be expected to be systematic (and consequently correlated) while they are assumed random and independent. Taken together, this leads to systematic errors ('biases') in the estimated fluxes. Many of the particular choices of the inversion set-up influence the result in a systematic way.

Partly, these biases can be assessed by performing sensitivity inversions, comparing the results of several inversions for which particular conditions are varied within a range compatible with contemporary understanding (the selection of sensitivity set-ups referred to later is specified in Table 4). Biases much smaller than the  $\pm 1\sigma$  intervals (68% probability ranges) can safely be ignored. On the other hand, if the results of the sensitivity inversions differ by more than  $\pm 1\sigma$ , the biases are obviously a dominant part of the uncertainty of the estimates. Naturally, biases that do not depend on any of the tested influences remain undetected by such a sensitivity study. For this reason, random errors and biases are not combined into a single uncertainty number here, which would unduly pretend a complete error quantification.

### 3. Results

At first, what added value can be expected from inversion-derived flux estimates, compared to a direct analysis of atmospheric CO<sub>2</sub> data? Taking the traditional zonally averaged perspective, Fig. 4 presents anomalies of the CO<sub>2</sub> history over latitude and time. As the information that drives the inversion, panel A shows the observed CO<sub>2</sub> growth rate anomalies. One recognizes anomalously high concentration increases associated with the El Niño events in 1983, 1988, 1998, and – less pronounced – 1994 (Conway et al., 1994; Keeling et al., 1995), as well as a period of reduced increase around 1991–1994, attributed by many authors to short-term climatic changes following the eruption of Mt. Pinatubo in June 1991 (Robock, 2002). Due to atmospheric mixing, which removes intrahemispheric concentration gradients on a time scale of weeks to



**CO<sub>2</sub> flux history  
1982–2001**

C. Rödenbeck et al.

Title Page

Abstract

Introduction

Conclusions

References

Tables

Figures

◀

▶

◀

▶

Back

Close

Full Screen / Esc

Print Version

Interactive Discussion

© EGU 2003

months and interhemispheric ones on a scale of about half a year (Maiss et al., 1996), the concentration signal is to a large degree diffused over the entire globe. By combining this signal with quantitative information on atmospheric transport, the inversion undoes part of this blurring: the resulting flux estimates (panel B) localize anomalies on a finer resolution. The tropics appear now as the main driver of the CO<sub>2</sub> growth rate anomalies, with the northern hemisphere midlatitudes coming next in importance. In panels C and D, the global flux has been divided into land and ocean contributions. As reflected in the different ranges on the color scales, variability on land is estimated to be approximately one order of magnitude larger than that on the ocean. That is to say, the global CO<sub>2</sub> anomalies are heavily dominated by the terrestrial processes.

We present our flux estimates on a variety of spatial and temporal scales. The different scales examined highlight different aspects of the result, discussed in Sects. 5 and 6 below. However, as explored in Sect. 4, they also differ markedly in their degree of credibility. The selection of scales, therefore, attempts to balance between the needs to answer the posed questions about the carbon cycle and the information that the inversion is able to provide.

### 3.1. Time variation of fluxes

Figure 5 shows time series of the estimated fluxes integrated over sets of regions tiling the globe. Fluxes have been deseasonalized by running annual summation, such that the temporal features represent a time scale of 1 year. The figure successively refines the spatial scale, covering the global flux total (part I), land and ocean flux totals (part II), 8 continental-scale regions (part III), and the TransCom3 tiling (Gurney et al., 2002, see Fig. 6) into 11 land regions (part IV) and 11 ocean regions (part V). The TransCom3 tiling is widely used, thus facilitating the comparison of our results with inversion estimates by other groups.

As noted above, the variability of global carbon fluxes (Fig. 5, part I) can be predominantly attributed to the land fluxes (part II). The estimated peak-to-peak amplitude of interannual variations is around 5 PgC/yr, equivalent to approximately 4% of the

amount ( $\approx 120$  PgC, IPCC, 2001) that is taken up globally by the photosynthesis of the terrestrial biosphere and released again by autotrophic and heterotrophic respiration every year. The main pace of the interannual variability on land is clearly determined by El Niño versus La Niña periods, the only exception being the Post-Pinatubo period of approximately two years duration. During El Niño there are large fluxes from land to the atmosphere, while during La Niña fluxes are directed towards the land. The 1997/1998 El Niño event caused the by far largest anomaly found during the two considered decades. No longer-term trend in land-atmosphere fluxes is readily discernible.

Looking at the breakup of the land fluxes into continental-scale regions (Fig. 5, part III), it can be seen that North American and Eurasian fluxes differ in their variability. In North America, fluxes vary over several-year periods, while in Eurasia they strongly fluctuate on a shorter time-scale (1 to 2 years, especially in its temperate sub-region, see part IV). One reason why Eurasia temperate fluxes are of a different character compared to North America temperate fluxes may be that several different climates influence the Eurasian temperate region while climate forcing is much more homogeneous over temperate and boreal North America (see Sect. 5). The ENSO signal appears to be reflected in the interannual variability of the Eurasian fluxes (in particular through the Eurasian Temperate sub-region [part IV] containing eastern and southern Asia) while this signal is not present in the North American fluxes. On the other hand, the North American region (particularly its temperate sub-region, see part IV) reacted particularly strongly to the changes that occurred after the Pinatubo eruption, in contrast to Eurasia.

Large variability strongly resembling the ENSO cycle is found in Tropical and South America as well as in Africa (Fig. 5, part III). In Africa, we also find a sudden large decrease in the net flux around 1989 (located in the southern sub-region, see part IV). We are not aware of any event that could be related to this feature, and tend to consider it as an artefact (see Sect. 4 below). In contrast to Tropical America and Africa, the variability for Tropical Asia and Australia is estimated to be modest, with a connection to ENSO being less apparent.

**CO<sub>2</sub> flux history  
1982–2001**

C. Rödenbeck et al.

[Title Page](#)[Abstract](#)[Introduction](#)[Conclusions](#)[References](#)[Tables](#)[Figures](#)[I◀](#)[▶I](#)[◀](#)[▶](#)[Back](#)[Close](#)[Full Screen / Esc](#)[Print Version](#)[Interactive Discussion](#)

**CO<sub>2</sub> flux history  
1982–2001**

C. Rödenbeck et al.

Title Page

Abstract

Introduction

Conclusions

References

Tables

Figures

◀

▶

◀

▶

Back

Close

Full Screen / Esc

Print Version

Interactive Discussion

© EGU 2003

The variability of the total ocean flux (Fig. 5, part II) differs more strongly than the land flux between the individual curves corresponding to the different station sets. This hints at limited robustness, to be discussed more systematically in Sect. 4 below. Excluding the large swings in the 11 stations case right after 1982, there does seem to be, however, a weak trend towards larger ocean uptake with time. Depending on the period considered, this trend is in broad agreement with the simple model where ocean uptake is proportional to the excess perturbation of the atmospheric CO<sub>2</sub> concentration caused by fossil fuel burning and cement production (0.1 to 0.6 PgC/yr per decade, Le Quéré et al., 2003).

The relatively small interannual variability of estimated ocean fluxes is in line with ocean model studies (Le Quéré et al., 2000), other atmospheric inversions (e.g. Bousquet et al., 2000; Rayner et al., 1999), and observations (e.g. Feely et al., 1999). Among the ocean fluxes in the three latitude bands of Fig. 5 (part III), the Tropics exhibits the largest variability. In the east of the tropical Pacific, ENSO related anomalies on the order of 0.5 PgC/yr are expected (Feely et al., 1999) which are however attributed by the inversion to a larger area (regions North Pacific Temp. and the summed West and East Pacific Tropics, part V).

### 3.2. Time-mean spatial distribution

Figure 7 presents long-term flux averages over different time periods. From top to bottom of the figure, the spatial resolution passes through the same succession of spatial scales as in Fig. 5. Even finer spatial scales are shown in Fig. 8 (panel (B)), depicting global maps of long-term mean flux estimates in the latest period of the inversion based on 35 stations.

Total carbon exchange of land and of ocean, respectively, are consistent within their uncertainty ranges with the a-priori values (Fig. 7, uppermost panel). At continental resolution (middle panels), we find carbon uptake in the tropical lands, of a surprisingly large magnitude in Tropical America. Uptake is also found in the northern hemisphere land regions, especially in America. Europe (in particular in its eastern part, see also

Fig. 8) is estimated to be a strikingly large source.

The latitudinal distribution of the ocean fluxes (Fig. 7, upper mid panel) show the expected pattern of outgassing in the tropics and uptake in the extratropics. In the south, however, the inferred uptake is considerably smaller than the a-priori estimate. Notable features at the regional scale (lowest panel, especially in the 35 stations estimate) are (1) less outgassing from the East Pacific Tropical region than expected from the a-priori estimates of Gloor et al. (2003), our estimates being more close to the estimates by Takahashi et al. (1999); (2) a much larger ocean carbon uptake in the South Pacific temperate region than expected from prior estimates; and (3) weak outgassing from the Southern Ocean.

### 3.3. Remark: The fossil fuel component

Emissions due to fossil fuel burning are generally considered the best-known component of the CO<sub>2</sub> budget, and are therefore usually subtracted from the results in order to focus on the less known components. We have followed this custom in this paper as well in all figures and numbers (unless explicitly stated otherwise). But, of course, the atmospheric CO<sub>2</sub> level is determined by the total flux, which is the quantity both relevant to climate and driving the inversion. It thus should be borne in mind that regions that appear in the time series, bar plots, maps, or tables as sinks may actually be CO<sub>2</sub> sources (see panel (C) of Fig. 8 in comparison to panel (B)).

### 3.4. Remark: Fit to the data

Consistency of the calculation requires that the concentrations modelled from the estimated a-posteriori fluxes (obtained by inserting  $f_{\text{post}}$  into Eq. (1) or – as an even more stringent test – by an independent forward simulation of the transport model) be, on average, within the  $\pm 1\sigma$  range from the observations  $c_{\text{meas}}$ . This is equivalent to the requirement that the part of the cost function  $\chi^2$  which corresponds to the data within the target period (excluding spin-up and ‘spin-down’ periods) be, per measurement,

Title Page

Abstract

Introduction

Conclusions

References

Tables

Figures

◀

▶

◀

▶

Back

Close

Full Screen / Esc

Print Version

Interactive Discussion

about or less than unity. In the standard run with 35 stations, we find  $\chi_c^2/n = 0.82$ , showing that the solution obtained indeed fits the data within the assumed uncertainties of measurements and model. Also, the normalized residuals were checked to fulfill the assumption of Gaussian error statistics.

## 4. Robustness

To what extent – and on which spatial and temporal scales – can we trust these results? This section tries to quantify the impact of possible error sources at the different scales examined. As mentioned in Sect. 2.3, this quantification will be based on the a-posteriori  $\pm 1\sigma$  intervals (containing all uncertainties that are accounted for a-priori) as well as a comparison of a range of standard and sensitivity inversions (revealing unaccounted for uncertainties). These measures of uncertainty are found in Fig. 9 (time series corresponding to Fig. 5), Fig. 10 (long-term values corresponding to Fig. 7), and panel (E) of Fig. 8 (long-term maps).

### 4.1. The station set

The impact of the choice of station set is tested by comparison of the five standard estimates in Fig. 5. In the overlapping periods, the flux estimates sometimes differ considerably. It is thus apparent that the geometry of the employed station network can affect the flux estimates in a systematic way. The differences between the lines show up predominantly as shifts in the long-term mean, while the timing and amplitude of flux anomalies is in rather good agreement for most regions (Fig. 5, parts IV and V). This is our incentive to adhere to homogeneous data records, as it means that the bias from the station set geometry (which is then nearly time-independent) does not spoil the time dependence of the derived fluxes. As a counter-example, Fig. 5 also includes an inversion based on all 42 stations of Table 1 ignoring any data inhomogeneity and different record lengths. As is particularly obvious in regions like ‘South Pacific Temper-

Title Page

Abstract

Introduction

Conclusions

References

Tables

Figures

◀

▶

◀

▶

Back

Close

Full Screen / Esc

Print Version

Interactive Discussion

**CO<sub>2</sub> flux history  
1982–2001**

C. Rödenbeck et al.

[Title Page](#)[Abstract](#)[Introduction](#)[Conclusions](#)[References](#)[Tables](#)[Figures](#)[I◀](#)[▶I](#)[◀](#)[▶](#)[Back](#)[Close](#)[Full Screen / Esc](#)[Print Version](#)[Interactive Discussion](#)

© EGU 2003

ate', this flux estimate 'jumps' between the different network biases every time a new station kicks in, thereby pretending trends and interannual variations that are absent in the estimates based on homogeneous records. Therefore, it is our view that only the estimates based on homogeneous data sets are suitable for interpretation of time variations.

Although the shifts in the long-term mean are the most pronounced effect, the different station networks also lead to a number of changes in the time-dependence, because any additional station can introduce additional patterns of temporal variability. Some pronounced features of the estimated flux history depend entirely on individual stations, the most important examples of which are listed in Table 5. Though such constellations do not at all mean that the concerned feature necessarily is an artefact, one should keep in mind that they are nevertheless more sensitive to possible problems with the measurements and/or the model at the respective station. In contrast, many other features are seen by several stations (indicated by the fact that they prevail irrespective of the removal of any individual station; only their amplitude might change), and may thus considered robust. Conversely, this discussion also warns us that we might be missing important temporal patterns due to the lack of a station in the right place.

It is natural to trust an estimate to a greater extent if it is based on more stations. The flux estimates based on 11 stations, for example, miss many of the patterns present in the cases with more stations (see in particular parts IV and V of Fig. 5). The 11 stations case is nevertheless included here to provide a homogeneous estimate over the entire target period (1982/01-2000/12). One should keep in mind, however, that many of those stations that are only present in the largest sets, may be associated with relatively large model representation errors (such as continental stations, cf. Sect. 2.2.3). Thus they also introduce a higher probability of artefacts (cf. Sect. 4.5 below). As an example, see the influence of the continental station BSC<sup>12</sup> given in Table 5 and further

<sup>12</sup> Although a similar situation could be expected at the nearby stations HUN and BAL, these only have a much smaller impact on 'Europe' (compare the 26 stations case (with HUN and

discussed in Sect. 5.

Therefore, we use the differences between the estimates based on 16, 19, 26, and 35 stations as a measure of the errors to be expected from the station set bias. Additionally, the difference to the inversion result based on 42 stations indicates the potential impact of those stations that were not included otherwise due to record inhomogeneities. Attention should be paid to the features mentioned in Table 5.

## 4.2. Unavoidable data gaps

In the selection of stations with sufficiently homogeneous records, small data gaps were permitted (Sect. 2.2.1). This reflects an attempt to balance the requirements of homogeneity and of a larger number of stations, given that the records of nearly all stations inevitably have at least occasional small gaps and varying measurement densities (Fig. 2). Since a data gap effectively means a change in the station network for one or a few months, it potentially leads to substantial artificial excursions on a monthly time scale (compare station set bias above). Note that, for example, since the Indian Tropical and Temperate Oceans are predominantly determined by the station SEY (Table 5) which was used despite the presence of some longer data gaps, these regions are particularly prone to problems of this type.

The average impact of data gaps can be quantified by a bootstrap test (Conway et al., 1994). In the inversion set-up of Rödenbeck et al. (2003), which is similar to set-up (b) in this study, such a test was done by forming an ensemble of 20 inversion runs using random selections of only 85% of the available monthly concentration values. The standard deviation of flux estimates across the ensemble was found to be up to about half the respective a-posteriori uncertainty interval. We conclude that remaining small data gaps permitted here are, overall, not a dominant error source.

Potentially, the impact of gaps might be reduced by introducing a-priori time correlations of a comparable scale (in addition to the space correlations), as tested in sensitivity studies (Conway et al., 2003; Rödenbeck et al., 2003; Rödenbeck et al., 2005; Rödenbeck et al., 2006; Rödenbeck et al., 2007; Rödenbeck et al., 2008; Rödenbeck et al., 2009; Rödenbeck et al., 2010; Rödenbeck et al., 2011; Rödenbeck et al., 2012; Rödenbeck et al., 2013; Rödenbeck et al., 2014; Rödenbeck et al., 2015; Rödenbeck et al., 2016; Rödenbeck et al., 2017; Rödenbeck et al., 2018; Rödenbeck et al., 2019; Rödenbeck et al., 2020; Rödenbeck et al., 2021; Rödenbeck et al., 2022; Rödenbeck et al., 2023; Rödenbeck et al., 2024; Rödenbeck et al., 2025) (BAL but without BSC) and the 35 stations case).

Title Page

Abstract

Introduction

Conclusions

References

Tables

Figures

◀

▶

◀

▶

Back

Close

Full Screen / Esc

Print Version

Interactive Discussion

ity set-up (d). Fig. 9 shows that differences are well in the range of other uncertainties. Note also that, since month-to-month variability has now been partly suppressed, the inversion seeks the fit to the data by increased space and year-to-year variability.

#### 4.3. Measurement errors

5 Random errors of the observed concentrations are accounted for in the a-posteriori  $\pm 1\sigma$  intervals. Systematic errors in the concentration data (e.g. long-term trends of measurement standards, or changes in sampling procedures) are eliminated as far as possible by extensive calibration procedures by the measuring institution (Conway et al., 1994; Masarie et al., 2001). On the part of the inversion, there is no possibility  
10 to either detect or correct remaining systematic influences.

#### 4.4. Atmospheric chemistry

Some systematic error is also introduced by the fact that the calculation is based on direct atmospheric CO<sub>2</sub> data only. However, the atmosphere also contains carbon as volatile organic carbon (VOC) emitted by the land biosphere, and CO from, e.g. fossil  
15 fuel and biomass burning, which are – while being transported – finally also converted into CO<sub>2</sub> (on a time scale of weeks to months). Thus, this can potentially lead to misattribution of CO<sub>2</sub> sources and sinks.

#### 4.5. Transport model

As for the measurement errors, part of the model representation errors are accounted  
20 for in the a-posteriori flux uncertainties. Again, however, this assumes random (and Gaussian) errors, while the transport model is expected to also misrepresent the concentration field systematically (e.g. offsets, too strong or too weak tracer dilution due to wrong mixing strength, missing temporal or spatial variability). Unfortunately, these biases cannot be assessed on the basis of the material available here. One possibility  
25 is to perform inversions with different transport models. Such an intercomparison

Title Page

Abstract

Introduction

Conclusions

References

Tables

Figures

◀

▶

◀

▶

Back

Close

Full Screen / Esc

Print Version

Interactive Discussion



**CO<sub>2</sub> flux history  
1982–2001**

C. Rödenbeck et al.

Title Page

Abstract

Introduction

Conclusions

References

Tables

Figures

◀

▶

◀

▶

Back

Close

Full Screen / Esc

Print Version

Interactive Discussion

© EGU 2003

was conducted by Gurney et al. (2002) for a similar (but non-interannual) inversion. They found model-to-model differences on the order of  $\pm 0.5$  PgC/yr for estimates of 5 year flux averages in TransCom land regions. This model spread ranged between approximately 0.5 to 1 times the mean a-posteriori uncertainty of these inversions. The transport model used here also took part in that intercomparison, giving flux estimates that differed from the inter-model mean by about 0.46 times the inter-model standard deviation. Unfortunately, the spread revealed in such an intercomparison study gives no indication of the difference between a particular model and reality. In particular, problems common to all contemporary models will remain undetected. This concerns, for example, drifts of the meteorological fields driving the transport models (e.g. due to changes in the meteorological observation network). An alternative to quantify (and even potentially correct) model biases would be the comparison of model simulations with measured concentrations of transport tracers with known surface source distribution. Though such tests with sulfur hexafluoride (SF<sub>6</sub>) and radon (<sup>222</sup>Rn) have been reported (Dentener et al., 1999; Denning et al., 1999; Heimann and Keeling, 1989; Jacob et al., 1997), no tracer species is currently available that offers a data set of sufficient spatial and temporal coverage as well as sufficiently accurate knowledge on the distribution of its sources and sinks.

Concerning the time-dependence of the model representation error, the maximum impact on the flux estimates could be quantified by a comparison with a case of a deliberately wrong time-dependence for the atmospheric transport, e.g. by driving the model with just one year's meteorological data used repeatedly for all years of the simulation. Such a comparison was done by Dargaville et al. (2000) and Rödenbeck et al. (2003) for different inversion techniques. For an inversion similar to that considered here, the latter study found differences between cases with several fixed meteorological years and with correctly varying year in the order of 1 PgC/yr (for a latitude band 15N-50N). If, as in this study, interannually varying meteorology (from a reanalysis data set produced with the same general circulation model throughout all the time period) is used, the actual error is expected to be much smaller than this maximum. This means

that the time-dependence of the model representation error is of minor importance. (Its impact on the long-term mean, however, is expected to be more severe.)

#### 4.6. Errors of a-priori fluxes

Errors of the a-priori fluxes are also accounted for in the a-posteriori  $\pm 1\sigma$  intervals.

5 As noted in Sect. 2.3, however, it should be checked if the actual error statistics are sufficiently well met. The consistency of the choices of Sect. 2.2.4 can be checked by replacing the prior flux  $f_{\text{pri}}$  by one of the various alternative choices available. By way of example, the sensitivity case (a) is based on different a-priori ocean fluxes (Table 4). According to Fig. 9, flux time series for the TransCom3 regions only shift their long-term  
10 values (remember that there is no interannual, only seasonal variability in the a-priori flux). These shifts follow closely the differences in prior estimates (Fig. 10, bottom panel). In contrast to the individual regions, the total ocean flux differs by less than 0.03 PgC/yr only, despite a 0.4 PgC/yr difference in the prior (top panel). This confirms the total ocean uncertainty, while it hints at the problem that the chosen correlation  
15 structure leads to too tight uncertainties at the smaller spatial scales. Therefore, a-posteriori flux uncertainties for these scales might be too small as well.

A similar situation is found in sensitivity case (e) changing the a-priori land fluxes (Table 4; Fig. 10, lower middle panel). Note in particular the behaviour of the Tropics. Though there are differences in the flux allocation among the individual tropical regions,  
20 the total tropical land flux is estimated fairly similar, despite the differences in the a-priori values.

The errors of the a-priori fossil fuel emission estimates (results by different authors differ both in total strength and trend and in geographical distribution) are part of the a-priori uncertainty intervals (Sect. 2.2.4). Nevertheless, as there is no fossil fuel component in the flux model (for the reasons given in Sect. 2.2.4), it has to be borne in  
25 mind that the inversion adjustments do not only contain biospheric or oceanic fluxes but possibly also a correction to the a-priori assumed fossil fuel flux.

Title Page

Abstract

Introduction

Conclusions

References

Tables

Figures

◀

▶

◀

▶

Back

Close

Full Screen / Esc

Print Version

Interactive Discussion

#### 4.7. Choice of flux model

As different approaches by different authors demonstrate (Fan et al., 1998; Rayner et al., 1999; Bousquet et al., 2000; Gurney et al., 2002; Bruhwiler et al., 2000), contemporary knowledge leaves sizable room for alternative choices in any inversion set-up.

5 Though the standard case of this study was designed according to what we consider the most plausible choices, some alternative cases may be similarly defensible. This first of all concerns the assumed prior uncertainty structure (magnitude, geographical distribution, correlations, see Sect. 2.1). It is essentially based on plausible proxies, rather than quantitative estimates; yet it has the potential to significantly influence the

10 spatial and temporal variation of the estimated fluxes. To quantify the robustness of our flux estimates towards these assumptions, a number of sensitivity tests have been performed (Figs. 9 and 10). As on comparing different station sets above, the results agree to a large extent in the timing of anomalies, but both long-term values and the amplitude of the anomalies differ. Largest changes were found when using large inver-

15 sion regions (b), partly as a consequence of the fact that implied a-priori uncertainties on the regional scale become larger (due to the fact that the a-priori uncertainties of the land and ocean totals are fixed). The changes caused by the alternative land uncertainty structure (c) (flat NEE uncertainty, a rather strong change with respect to the standard set-up) generally remain within the  $1\sigma$  intervals; the largest effect here is a shift of fluxes between 'Tropical Asia' and 'Australia'. Further tests, such as doubled

20 ocean uncertainty (f), showed similar or smaller effects (not shown). In particular, details of the fossil fuel part of the flux model (e.g. setting the total fossil fuel uncertainty to zero in place of 0.37 PgC/yr) have hardly any influence on the results (not shown).

#### 4.8. Spatial scales

25 The degree of robustness of the inversion results depends on the spatial scale over which fluxes are integrated. Since the information present in the flux estimates can only reflect the information that was input into the inversion, the minimal spatial scale

Title Page

Abstract

Introduction

Conclusions

References

Tables

Figures

◀

▶

◀

▶

Back

Close

Full Screen / Esc

Print Version

Interactive Discussion

**CO<sub>2</sub> flux history  
1982–2001**

C. Rödenbeck et al.

Title Page

Abstract

Introduction

Conclusions

References

Tables

Figures

◀

▶

◀

▶

Back

Close

Full Screen / Esc

Print Version

Interactive Discussion

© EGU 2003

still constrained by the data is determined by the spatial resolution of the concentration field, as roughly determined by the distances between the atmospheric stations. This is illustrated in Fig. 8 (F). The reduction in uncertainty so shown is a measure of the ability of the inversion to constrain the flux in that location by measurements (Tarantola, 1987): A value of zero indicates that a location is only determined by the a-priori flux, while a value of one would correspond to a hypothetical complete constraining of the result by the data (only possible for zero data uncertainty and in the absence of atmospheric mixing). We recognize that an appreciable impact of the inversion on the fluxes is only possible in the vicinity of the employed stations, where the radius of influence reflects both the scale of atmospheric mixing and the range of spatial correlations that was applied. Even in the relatively well constrained northern hemisphere mid-latitudes where the station density is largest, the reduction of uncertainty is therefore rather uneven, while most tropical regions are poorly constrained throughout. Nevertheless, the reduction of uncertainty of regionally integrated fluxes (ratio between a-posteriori and a-priori  $\pm 1\sigma$  intervals depicted in Fig. 9) indicates that these larger scales are reasonably well constrained. The apparent paradox is resolved by realizing that, even if the partition of fluxes between subregions should be wrong, the sum might nevertheless be correctly inferred (e.g. due to a-posteriori anti-correlations between the subregions). Reverting this conclusion, flux adjustments in the constrained areas can be exaggerated as a compensation for less constrained areas in order to satisfy the larger-scale constraints imposed by the data. Although the shape factors (Sect. 2.2.4) try to maintain a reasonable spatial structure even at the small scales, it can be seen that unrealistic fluxes in locations such as the Gobi desert are estimated, despite the low a-priori uncertainty there. Therefore, spatial details in the flux estimates of Fig. 8 should be looked at with great caution.

In accordance with this consideration, the measures of uncertainty discussed in the previous subsections generally increase when going from the largest spatial scale to the break-up into 22 TransCom3 regions. As an example, the individual long-term values for 'Australia' and 'Tropical Asia' (Fig. 7, third Panel) depend much more on the

chosen set-up than their (larger-scale) sum 'TrAsia+Australia' (second Panel), revealing that the sub-partition is only uncompletely resolved. Further, we notice in Fig. 5 (part V) that the regions 'Indian Tropical Ocean' and 'S Indian Temp. Ocean' essentially exhibit the same time variability, showing that these two regions do not contain independent information. The same is true to a smaller extent for the pair 'East Pacific Tropics' and 'South Pacific Tropics', as well as for the three Atlantic regions.

#### 4.9. Time scale

In the space dimension, the flux estimates were found to generally be the more robust, the larger the scale of integration (averaging) that is chosen. In the time dimension, the situation differs: Since most of the discussed error sources mainly lead to time-independent biases that do not affect time variations of the fluxes, the long-term spatial distribution of fluxes (i.e. the largest time scales) are most strongly affected. Also, long-term trends turn out to be less robust (see, e.g. 'South American Tropical'). In addition, sudden changes such as that in 'Southern Africa' in 1989 or various ones in 'West Pacific Ocean' seem doubtful (see Table 5). Since particular problems in these cases could not be identified (and potentially solved), we generally tend to consider features on time scales greater than about 10 years with caution.

The space and time dimensions also differ in their respective smallest scales: While the spatial resolution of the fluxes (730 regions globally) is much finer than that of the data (network of maximally 35 stations globally), the finest time resolution of data and fluxes is equal (one month). Nevertheless, one cannot expect month-to-month variations of the flux estimates to be correct because these are heavily affected by the remaining data gaps (Sect. 4.2) or by possible problems with the measurements or the model simulation in individual months. Seasonal information, therefore, needs to be considered with care. In the present paper, we restrict ourselves to deseasonalized fluxes (yearly sum).

When looking at temporal features in the time series plots, it should be kept in mind that peak heights can only be considered relative to each other because the absolute

Title Page

Abstract

Introduction

Conclusions

References

Tables

Figures

◀

▶

◀

▶

Back

Close

Full Screen / Esc

Print Version

Interactive Discussion

amplitude of the variations strongly depends on the (somewhat arbitrary) degree of smoothing applied to the figures, as well as on the time correlation length.

#### 4.10. Summary: How much can we believe?

- Timing and relative strength of anomalies in time (scale 1.5 to 10 years) constitute the most robust part of the result (compare [Bousquet et al., 2000](#)). This can be understood because the majority of error sources have no or only a little systematic time dependence.
- The long-term-average spatial distribution of fluxes depends sensitively on many poorly constrained factors. It should be interpreted with great care.
- Concerning anomalies, the systematic biases revealed by differences between inversion results generally remain compatible with the 68% range given by the a-posteriori uncertainty intervals. Biases of long-term fluxes at higher spatial resolution can be much larger than  $\pm 1\sigma$  (e.g. in South American Temperate as well as South and East Pacific Tropics).
- Robustness improves with an increasing number of stations (compare both the  $\pm 1\sigma$  intervals and the spread between the different sections in time of Fig. 9).
- A number of errors (model representation error, range of choices of flux model) can only be partially quantified. Comparison with flux estimates from independent methods as discussed in Sect. 5 below suggests however that they do not overwhelm the result.

## 5. Discussion - Time mean picture

Keeping in mind that the long-term flux pattern can be estimated by the inversion with less confidence only than the time variability, the discussion of the time mean picture

Title Page

Abstract

Introduction

Conclusions

References

Tables

Figures

◀

▶

◀

▶

Back

Close

Full Screen / Esc

Print Version

Interactive Discussion

is focussed on the comparison of the present findings with estimates by a variety of independent methods, as well as earlier studies that inferred CO<sub>2</sub> fluxes using atmospheric data.

### 5.1. Land/Ocean breakdown

5 We start with a comparison of the estimated land/ocean breakdown with that inferred from changes in atmospheric O<sub>2</sub> and CO<sub>2</sub> (Keeling and Shertz, 1992). The estimates used here (Bopp et al., 2002; Keeling and Garcia, 2002; Plattner et al., 2002, Table 6,) involve a correction taking into account ocean-atmosphere oxygen fluxes caused, e.g. by warming of the oceans (Levitus et al., 2001). Despite such complications we view  
10 the oxygen approach as the most reliable amongst the existing methods, because it addresses the partitioning of land and ocean carbon fluxes in a direct and conceptually simple way.

To permit a comparison of the net ocean-atmosphere carbon flux estimated by the two methods, riverine carbon transport needs to be taken into account<sup>13</sup>. The compar-  
15 ison then reveals an overall agreement within the uncertainty ranges of the methods.

<sup>13</sup> The ocean/atmosphere flux estimated by the inversion is the total net CO<sub>2</sub> flux through the air-sea interface. This includes the oceanic branch of the riverine carbon loop which is directed from the ocean to the atmosphere (Sarmiento and Sundquist, 1992). The O<sub>2</sub>/N<sub>2</sub> method, by contrast, separates the trend of atmospheric carbon not explained by fossil fuel emissions into an exchange flux between atmosphere and biomass (essentially into CH<sub>2</sub>O) and a remainder. The remainder is the carbon flux through the air-sea interface without any contributions from the oceanic branch of the riverine carbon loop, because the land and oceanic branches effectively cancel out. Underlying assumptions are that both the organic carbon pool in the ocean and the riverine carbon loop prevail in a steady state.

The magnitude of river carbon fluxes is taken here from Ludwig et al. (1996). They obtained a riverine transport of 0.4 PgC/yr of organic carbon and of 0.41 PgC/yr of inorganic carbon of which 0.2 PgC/yr are eventually buried in the ocean sediments as CaCO<sub>3</sub>. In the estimates based on the O<sub>2</sub>/N<sub>2</sub> method in Table 6, therefore, an amount of 0.6 PgC/yr has been reallocated from ocean to land, with the original numbers given in parantheses.

Title Page

Abstract

Introduction

Conclusions

References

Tables

Figures

◀

▶

◀

▶

Back

Close

Full Screen / Esc

Print Version

Interactive Discussion

**CO<sub>2</sub> flux history  
1982–2001**

C. Rödenbeck et al.

Title Page

Abstract

Introduction

Conclusions

References

Tables

Figures

◀

▶

◀

▶

Back

Close

Full Screen / Esc

Print Version

Interactive Discussion

© EGU 2003

The agreement is particularly close for the 1980's while for the 1990's our estimates indicate a slightly larger ocean sink than estimated from the O<sub>2</sub>/N<sub>2</sub> ratio. A slightly larger sink is also more in line with the results from a recent study of McNeil et al. (2003) based on the invasion history of CFCs into the oceans.

To judge to what extent this encouraging result on the global partitioning between ocean and land fluxes is induced by the prior estimates, we used, in sensitivity case (a), the ocean/atmosphere fluxes as estimated by Takahashi et al. (1999) as priors instead of the Gloor et al. (2003) fluxes (Fig. 10, top panel). The difference in global ocean uptake between these prior fluxes is 0.4 PgC/yr, nevertheless the estimate for global ocean uptake hardly changes. This gives us some confidence that the method indeed possesses an ability to distinguish between land and ocean carbon exchange on a global scale with an uncertainty similar to that of the O<sub>2</sub>/N<sub>2</sub> approach.

## 5.2. Rough Northern Hemisphere/Tropics/Southern Hemisphere breakdown

Slightly increasing the spatial resolution, we now consider the breakdown of land/ocean sources and sinks into a northern extratropical hemisphere, a tropical band (approximately 20° S to 20° N) and a southern extratropical hemisphere (Table 7). For both periods considered (01/1992–12/1996 and 01/1996–12/1999), we find a northern hemisphere land sink of about 0.5 PgC/yr and a tropical land sink of about 1 PgC/yr. Southern hemisphere land regions are approximately in balance. The ocean uptake is confined to mid and high latitudes while there is carbon outgassing from the tropics. This is expected from both the upwelling of nutrient-rich waters from intermediate depths and the entrainment of waters from the subtropics (Feely et al., 1999). Ocean uptake tends to be larger in the Northern than in the Southern hemisphere, in contrast to the estimates by Takahashi (2002) based on measurements of CO<sub>2</sub> partial pressure differences. Even if Takahashi et al. (1999)'s estimates are used as ocean a-priori flux, this disagreement prevails (Fig. 10, sensitivity case (a)). Though less pronounced, larger ocean uptake in the northern hemisphere compared to the Southern hemisphere was also found by the (non-interannual) inversion intercomparison study Transcom3 (Gur-



ney et al., 2002).

Taking land and ocean together, we find a difference between the fluxes of the two extratropical hemispheres of approximately 1 PgC/yr. This difference is substantially smaller than estimated by Transcom3 (Gurney et al., 2002) where a difference of 2.3 PgC/yr was found (Table 7). The difference results mainly from reduced northern hemisphere land uptake and larger tropical land uptake as estimated by our inversion. According to the Transcom3 experiments, this latitudinal shift in land uptake cannot be attributed to any anomalous transport properties of our transport model TM3 which took part in that intercomparison (Gurney et al., 2002). We note also that our tropical land flux estimates vary considerably between different time periods and different inversion configurations (Table 7, Figs. 7 and 10). Nevertheless, the sign of the fluxes is mostly the same (a net sink for atmospheric CO<sub>2</sub>). As already discussed, the reason for the scatter is likely the insufficient data coverage in the tropics. It should also be noted again that our standard inversion set-up allows much ‘freedom’ for tropical fluxes due to large a-priori uncertainties; lower uncertainties – as in sensitivity case (c)– lead to a smaller magnitude in the estimated sink (Fig. 9). Different results between Transcom3 and the present inversion are likely due to methodological differences. TransCom3 uses annual mean CO<sub>2</sub> data, taking the biospheric seasonality into account by pre-subtracting the simulated concentration response (rectification effect) of a seasonally varying a-priori flux, while for the time-dependent inversions as performed here, the seasonality of the fluxes is explicitly solved for. Therefore, at this stage we can only state that our results imply a smaller northern hemisphere land sink than inferred by annual mean atmospheric CO<sub>2</sub> data and models.

### 5.3. 8 and 22 regions breakdown

Increasing the spatial resolution of fluxes to the continental and sub-continental scales, we find that the land carbon uptake attributed to the tropics is due to estimated uptake in the Tropical Asian and South American Tropical regions (Fig. 7). As discussed in Sect. 4.6, however, we do not have great confidence in the breakdown of the tropical

Title Page

Abstract

Introduction

Conclusions

References

Tables

Figures

◀

▶

◀

▶

Back

Close

Full Screen / Esc

Print Version

Interactive Discussion

**CO<sub>2</sub> flux history  
1982–2001**

C. Rödenbeck et al.

Title Page

Abstract

Introduction

Conclusions

References

Tables

Figures

◀

▶

◀

▶

Back

Close

Full Screen / Esc

Print Version

Interactive Discussion

© EGU 2003

land flux. It is difficult to assess the realism of the inferred net carbon uptake on the order of  $-0.6 \pm 0.3$  PgC/yr in the South American Tropical region over the decade of the 1990s (Fig. 7, lower middle panel). It should be stressed that the inversion estimates the total (net) surface-atmosphere flux, which in this area consists of two large components of opposite sign: a CO<sub>2</sub> release from changes in land use (mostly from deforestation, Houghton et al., 2003), and a carbon uptake by the remaining natural ecosystems (e.g. Phillips et al., 1998) and in regrowing secondary forests on abandoned, previously deforested areas (DeFries et al., 2002). Recent assessments based on remote sensing data have yielded a deforestation source in tropical South America ranging from 0.2 to 0.7 PgC/yr (DeFries et al., 2002). The overall net uptake inferred by the inversion thus would imply an uptake in natural ecosystems of  $-0.8$  to  $-1.3$  PgC/yr.

The land sink in the northern hemisphere is attributed by our inversion to North America (Fig. 7, upper middle panel). For the 11 TransCom3 land regions (lower middle panel), we find approximately equally large sinks in boreal and temperate North America, a source in Europe, and a roughly balanced carbon budget in Eurasia. This longitudinal asymmetry in the northern hemisphere is not supported by estimates from inventory-based carbon accounting studies. For example, Kurz and Apps (1999) reported a longterm average of  $-0.2$  PgC/yr for Canada during 1920–1989, while Shvidenko and Nilsson (2003) presented a conservative estimate of  $-0.42 \pm 0.07$  PgC/yr for Russia (1961–1998) including land-use change and peatland dynamics (Nilsson et al., 2000). Nevertheless, the much larger east-west extension of the Eurasian boreal region (and the resulting more extremely continental climate) compared to the Canadian boreal region could indeed play a role. As a consequence, permafrost areas in Siberia are larger, which could for example affect decomposition processes related to permafrost thawing. Besides this, while the northern hemisphere high latitude regions have warmed by approximately  $0.8^\circ$  C over the last 30 years there are asymmetries in the warming rates between the regions (Serreze et al., 2000), tendentially with stronger warming in Eurasia (compare also Zhou et al., 2001). One should keep in mind, however, that a strong latitudinal asymmetry is involved also in the inversion calculation

itself, due to substantially different station densities.

To document what leads the inversion to conclude on a European CO<sub>2</sub> source it is helpful to consult atmospheric data that are aligned roughly along longitude circles in the West and the East, respectively (Fig. 11). While the CO<sub>2</sub> data exhibit a West-East increase, as would be expected, the conclusion on a source based on these data hinges on the magnitude of the fossil fuel signal and the realism of the simulation of this signal with the atmospheric transport model. Unfortunately, we do not currently have convincing, independent evidence (e.g. from transport tracers) to check how realistic the simulated transport really is. The data that is predominantly responsible for the Eastern European carbon source is from the station BSC (Black Sea, Constanta), Table 5. This station does not only record so-called background air with only “small” CO<sub>2</sub> short term (hours to days) variability but there are also large deviations from the background that are likely due to plumes from fossil fuel burning (see the spikes occurring both in the data and in the simulated fossil fuel response). Though one might therefore expect the errors of the station data to deviate from a Gaussian distribution, any violation of this assumption underlying the method was not found (Sect. 3.4) even at BSC. Only the mean relative residual at BSC is significantly different from zero, which can be interpreted as a correction for a systematic model representation error.

In a similar situation, the large carbon uptake in the South Pacific temperate region is caused by the data from the Easter island station (EIC) that are compared with data from a few selected stations in Fig. 12. Once the simulated fossil fuel signal is subtracted from the data it is apparent that the CO<sub>2</sub> concentration at the Eastern island station is lower than at adjacent stations both to the north and the south. As the Eastern island station is located suitably to capture air from a large ocean footprint it is well possible that there is some reality to the ocean sink signature indicated by these data.

CO<sub>2</sub> flux history  
1982–2001

C. Rödenbeck et al.

Title Page

Abstract

Introduction

Conclusions

References

Tables

Figures

◀

▶

◀

▶

Back

Close

Full Screen / Esc

Print Version

Interactive Discussion

## 6. Discussion – Drivers of short-term flux variability

For a rough investigation of the relation between short-term responses of ecosystems on continental and sub-continental scales to the varying climate, we discuss in the following flux anomalies for events representative for the main modes of interannual variations: El Niño (here the 1997/1998 event), La Niña (here the period from 10/1998 to 09/1999) and the two-year 'Post Pinatubo' period (06/1991 to 05/1993). For the calculation of flux and climate anomalies we had to compromise between record length and the robustness of the determination of flux anomalies. We decided to use flux estimates based on 19 stations which span a 10 year period, and to consider climate anomalies with respect to the same period. However, we restrict the analysis on the most recent El Niño and La Niña events only, as they permit some control on the flux dependence on the network.

As biomass burning potentially contributes to the large increases of the growth rates of atmospheric carbon during El Niño periods (Page et al., 2002), we finally compare our flux estimates with satellite-derived fire counts.

Main limiting factors for Net Primary Productivity (NPP) are temperature, water availability, light, nutrients (mainly nitrogen and phosphorus) and disturbances altering the ecosystem structure. Limitations for NPP are thought to vary with latitude and to a lesser degree with longitude and depend on the time span of the responses considered. At high latitudes the main limiting factor on time-scales on the order of one year is thought to be temperature. At temperate mid latitudes, water and light limitation become increasingly important, while at lower latitudes with Steppe and Savanna vegetation precipitation becomes the dominant limiting factor. For tropical rain forests light, water, and possibly carbon are thought to be limiting but which one dominates on a large spatial scale is uncertain. In addition, increases in the relative fractions of diffuse over direct light induced by the stratospheric aerosol after the Pinatubo volcanic eruption have been proposed to enhance NPP (Roderick et al., 2001).

Microbial respiration increases with temperature (Rustad et al., 2001) according to

Title Page

Abstract

Introduction

Conclusions

References

Tables

Figures

◀

▶

◀

▶

Back

Close

Full Screen / Esc

Print Version

Interactive Discussion

the Arrhenius' equation (Lloyd and Taylor, 1994; Kirschbaum, 1995). Microbial activity in soil increases also with humidity as long as the soils are not water saturated (Larcher, 1994).

Finally the conditions that are necessary for or favor the occurrence of fires are (i) droughts (i.e. a water deficit), (ii) high temperatures, (iii) availability of fuel and (iv) ignition sources (Johnson, 1992).

## 6.1. Flux response to climate anomalies

For each of the three events considered, we now summarize the observed deviations of precipitation and temperature from the mean climate (upper and middle panels of Figs. 13, 14, and 15, respectively). We then describe the corresponding features found in our flux estimates (lower panels), and discuss the implications of the comparison.

### 6.1.1. Post-Pinatubo period

Compared to the El Niño and La Niña periods discussed below, climate anomalies were comparably small after the eruption of Mt. Pinatubo (Fig. 13). Largest precipitation anomalies occurred in Amazonia south from the equator, covering large parts of the tropical rain forest. Precipitation anomalies, albeit of a lesser magnitude, were also observed in large parts of the rest of the tropics while there was anomalously low precipitation throughout Eurasia. Globally, temperatures were mostly cooler. Eastern and South-eastern North America experienced slightly wetter and cooler conditions.

Nevertheless, the Post-Pinatubo period is the one with the largest anomalous growth rate of atmospheric CO<sub>2</sub> observed so far with direct measurements. Curiously, according to our estimates the distribution of anomalous carbon uptake regions across the globe is markedly uneven. The regions that are mainly responsible for enhanced carbon uptake are the Amazon basin and the East of North America. For the rest of the world, flux anomalies are small.

Comparison of these flux anomalies with the climate anomalies indicates that in-

Title Page

Abstract

Introduction

Conclusions

References

Tables

Figures

◀

▶

◀

▶

Back

Close

Full Screen / Esc

Print Version

Interactive Discussion

creased carbon uptake tends to coincide with increased precipitation, although the comparison is not entirely conclusive. While our result does not rule out the hypothesis by Roderick et al. (2001) of an overall stimulation of photosynthesis by the increased diffusive light fraction as an important mechanism, it suggests that this mechanism does not suffice as an explanation on its own. This is because anomalous carbon uptake is distributed very unevenly across the globe.

### 6.1.2. 1997/1998 El Niño event

As a consequence of the horizontal shifts of the atmospheric regions with deep convection in the tropics, large changes in precipitation on land are observed (Fig. 14). This concerns particularly large parts of tropical South America and parts of Indonesia where precipitation is strongly reduced. In addition, a dipole type precipitation anomaly in China is observed.

There was a strong asymmetry of the temperature at northern hemisphere high latitudes which strongly elevated values in North America (up to 2° C) but strongly reduced values in Siberia. Warmer temperatures were also observed throughout the tropics with largest values in tropical South America.

Carbon flux anomalies during 06/1997–05/1998 are dominated by very large carbon losses from tropical South America and the region centered around Indonesia. Northern hemisphere flux anomalies are out of phase with the tropical fluxes and are of a much smaller magnitude.

The large carbon losses from the tropical land regions coincide very well with the precipitation anomalies while temperature anomalies alone, as observed for Central Africa, seem not to be sufficient to lead to significant flux anomalies.

It is interesting that the large positive temperature anomalies at northern hemisphere high latitudes are not reflected in any obvious way in the flux estimate record, somewhat contrary to what is expected. A reason may be that responses to temperature anomalies in these regions operate on longer time scales than one year.

Title Page

Abstract

Introduction

Conclusions

References

Tables

Figures

◀

▶

◀

▶

Back

Close

Full Screen / Esc

Print Version

Interactive Discussion

### 6.1.3. 1999 La Niña period

Larger precipitation rates in the period 10/1998–09/1999 compared to usual prevailed in Central America and South America north of approximately 10° S (Fig. 15). As for the Post-Pinatubo period, the anomaly in South America covers a large part of the Amazonian rainforest. Regions with reduced precipitation is Eastern North America, the region in South America adjacent to the tropics, large parts of Central Africa and to a lesser degree Indonesia.

Temperature anomalies for Eurasia, Africa, Australia, and North America were roughly similar as the anomalies during the 1997/1998 El Niño: lower temperatures in Siberia, higher temperatures North America at high latitudes (with exception of the West coast) and higher temperatures in the tropics. Temperature anomalies are different in South America, however, where anomalies are negligibly small.

Compared to both the Post-Pinatubo and the 1997/1998 El Niño period, flux anomalies are smaller. Largest anomalies are estimated in tropical South America with anomalously large carbon uptake and the Indonesian region with anomalously large carbon losses. Anomalies of a lesser magnitude are also observed throughout Siberia (carbon outgassing) and Central Africa.

The anomalous fluxes from tropical South America and Indonesia are consistent with the picture of increased/decreased CO<sub>2</sub> fluxes for decreased/increased precipitation (and, at least for Indonesia, increased/decreased temperatures). In contrast, the flux anomalies from Siberia and Central Africa are difficult to understand. Partly, this may also be due to the limited spatial resolution of the inverse calculations, and the limitation of our comparison to annual climate anomalies.

Similar as for the El Niño phase, there is hardly any response to temperature anomalies at northern hemisphere high latitudes in North America, despite the large observed temperature anomalies.

Title Page

Abstract

Introduction

Conclusions

References

Tables

Figures

◀

▶

◀

▶

Back

Close

Full Screen / Esc

Print Version

Interactive Discussion

#### 6.1.4. Summary

The most variable and significant region for anomalous fluxes on a global scale for all three events considered here is the tropical South American region. Two regions that are next in importance are the Indonesian and the Eastern North American region. The dominant driver for the flux anomalies in the tropics seem to be precipitation anomalies that may be amplified by temperature anomalies. This is in line with the model results by Tian et al. (1998).

Despite large temperature anomalies at northern hemisphere high latitudes there is no obvious connection to flux anomalies there, as would be expected from the temperature dependence of soil respiration.

While precipitation anomalies are roughly compatible with the anomalously large fluxes observed during the Post-Pinatubo period, a striking feature during this period is the uneven distribution of source and sink anomalies over the globe.

#### 6.2. Biomass burning

Finally, we compare firecounts from the ATSR World Fire Atlas (European Space Agency – ESA/ESRIN, Frascati, Italy, <http://shark1.esrin.esa.it/ionia/FIRE/AF/ATSR/>) with the observed time course of the flux estimates (Fig. 16). These fire count statistics are available from 1997 onwards. Particularly large (“anomalous”) fires raged during September/October 1998 in Eastern Siberia (Jakutia), in Indonesia and Indochina in 1997 and 1998, and in May 1997 in Central America. The comparison of the flux estimates with the satellite based fire count histories reveals a particularly good correspondence for Indonesia and Australia. In particular the 1997/1998 fire event in Indonesia seems well captured by the inverse estimates. Furthermore, the flux anomaly of  $\approx 1$  PgC/yr estimated by the present inversion is within the range of the flux estimates of Page et al. (2002) based on remote sensing data and ground-based assessment, albeit rather at the lower end. A reasonably good correlation is also found in tropical South America, Central America and Eastern Siberia. This points towards fire as an impor-

Title Page

Abstract

Introduction

Conclusions

References

Tables

Figures

◀

▶

◀

▶

Back

Close

Full Screen / Esc

Print Version

Interactive Discussion



tant player in the large releases of carbon during El Niño events, albeit the exact role is not possible to determine with this method. In the remaining regions, no convincing correlation is obtained.

The surprisingly close correlation of carbon fluxes and fire counts recorded by satellites in several regions for which biomass burning is thought to play a significant role for carbon release, is encouraging evidence that the inverse method is able to capture and localize large carbon flux events not contained in the a-priori estimates. On the other hand, this tentatively provides an independent quantification of biomass burning fluxes. Furthermore, the magnitude of the fire fluxes as estimated by the inverse method (that probably tends to underestimate them because they represent a large deviation from the a-priori fluxes) is compatible with the hypothesis that fires contribute substantially to anomalously large carbon fluxes to the atmosphere during El Niño events. This is in agreement with the analysis of [Page et al. \(2002\)](#) mentioned above, and [Langenfelds et al. \(2002\)](#) that employed atmospheric concentration records of CO, CH<sub>4</sub> and H<sub>2</sub> in addition to CO<sub>2</sub> for the same purpose.

## 7. Summary and outlook

The recent CO<sub>2</sub> flux history was reconstructed using a time-dependent inverse approach based on atmospheric concentration data and observed winds. Major findings and conclusions can be summarized as follows:

1. The inverse method is suited for estimating the temporal variability of CO<sub>2</sub> fluxes on continental to sub-continental scales.
2. In agreement with previous studies, land fluxes are estimated to be the main driver of interannual variations in atmospheric carbon content, with the pace predominantly being set by the El Niño/La Niña contrast. An exception is a 2-3 year period of increased sink of atmospheric carbon after Mt. Pinatubo's volcanic eruption in

Title Page

Abstract

Introduction

Conclusions

References

Tables

Figures

◀

▶

◀

▶

Back

Close

Full Screen / Esc

Print Version

Interactive Discussion

**CO<sub>2</sub> flux history  
1982–2001**

C. Rödenbeck et al.

Title Page

Abstract

Introduction

Conclusions

References

Tables

Figures

◀

▶

◀

▶

Back

Close

Full Screen / Esc

Print Version

Interactive Discussion

© EGU 2003

1991. The largest differences in fluxes between El Niño and La Niña are found in the tropical land regions, the main share being due to Tropical South America.

3. As the variations of fluxes due to El Niño, La Niña and Post-Pinatubo effects are very distinct, they can be used to identify relationships between climatic variability and induced CO<sub>2</sub> flux variability and to investigate the underlying mechanisms.

The rough analysis presented here suggests that the short-term variability of tropical biospheric fluxes is strongly related to precipitation anomalies.

4. The timing of several large biomass burning events in the recent past is captured by the inversion, as demonstrated by comparison with fire counts from satellites. This comparison confirms that fires are an important mechanism of carbon release to the atmosphere during El Niño phases.

5. There is a weak long-term trend towards increased uptake by the global oceans (in particular in the Northern hemisphere) that is consistent with the trend expected from rising atmospheric CO<sub>2</sub> concentration. On land, no long-term trend is found.

6. The estimated long-term spatial flux patterns might be affected by substantial systematic errors.

Nevertheless, the estimated partitioning of uptake of anthropogenic carbon by oceans and land agrees well with that inferred from the observed trend in the O<sub>2</sub>/N<sub>2</sub> ratio.

Tentatively summarizing the estimated long-term spatial distribution of fluxes (01/1996–12/1999), we find a northern hemisphere land sink of only 0.4 PgC/yr which is substantially smaller than the results from most previous studies (IPCC, 2001; Gurney et al., 2002). We also find a smaller difference (on the order of 1 PgC/yr) between uptake in the two hemispheres compared to these studies. This is mainly due to a shift in land uptake of carbon from the northern hemisphere to the tropics, with an estimated tropical land sink of 0.8 PgC/yr.

**CO<sub>2</sub> flux history  
1982–2001**

C. Rödenbeck et al.

Title Page

Abstract

Introduction

Conclusions

References

Tables

Figures

◀

▶

◀

▶

Back

Close

Full Screen / Esc

Print Version

Interactive Discussion

On a continental scale, Eurasia is approximately carbon balanced while North America is a carbon sink. There is larger ocean carbon uptake in the South Pacific temperate region than expected from prior estimates and weak outgassing from the Southern Ocean.

5 Though details of the inversion method could potentially be modified or refined, we believe that qualitatively more valuable results can only be achieved through a higher density of atmospheric data, possibly also including additional sources of information. Satellite data are a way to dramatically increase the spatial resolution (Houweling et al., in preparation). At present, the SCIAMACHY and AIRS instrument are measuring CO<sub>2</sub> from space, and data are expected to become available in the coming years. Due to the limited lifetime of satellites and calibration issues, they are expected to be particularly suitable for short-term studies. Alternatively, continuous CO<sub>2</sub> analysers provide a strongly increased data density in time. Together with highly resolved (regional) models of atmospheric transport, this could potentially exploit the information contained in ‘synoptic events’ (Law et al., 2002). For example, concentration peaks associated with fronts might be related to the sources and sinks along the particular trajectory of the weather system. Currently, success of this approach might be limited by the realism of available regional transport models. As a further possibility, the isotopic composition of CO<sub>2</sub> (such as <sup>13</sup>CO<sub>2</sub>, <sup>14</sup>CO<sub>2</sub>, CO<sup>18</sup>O) could be exploited. So far, however, this approach has not been very successful, owing to the fact that the increase of exploitable observational evidence is accompanied by an even larger increase in the number of unknowns. This is due to the highly complex mechanisms of isotopic fractionation that determines the characteristic isotopic signature of a particular CO<sub>2</sub> source or sink. Finally, one could also increase information on the model side, by using detailed process-oriented flux models that incorporate the available process understanding in a more direct way. Success of this approach, however, will crucially depend on as many yet open questions, such as the variability of model parameters in space and time, the realism of the model, or its degree of non-linearity.

**CO<sub>2</sub> flux history  
1982–2001**

C. Rödenbeck et al.

Title Page

Abstract

Introduction

Conclusions

References

Tables

Figures

◀

▶

◀

▶

Back

Close

Full Screen / Esc

Print Version

Interactive Discussion

© EGU 2003

Notwithstanding these perspectives, inversions of the type presented here are a valuable tool to monitor long-term variations of the global carbon cycle. In our opinion, therefore, continuation of the world-wide flask sampling program should remain a high priority of carbon cycle research. We particularly stress the importance of homogeneous long-term data records, as shown in this paper. Any extension of the station network by stations that provide unsmoothed data calibrated against a well-defined scale, would help to improve the robustness and spatial resolution of flux estimates, enhancing their value in the understanding of the carbon cycle and its changes.

*Acknowledgement.* We are obliged to P. Tans, T. Conway, and their coworkers at National Oceanic and Atmospheric Administration/Climate Monitoring & Diagnostics Laboratory (NOAA/CMDL), whose measurement efforts and well-documented data base are the basis of the presented flux estimates. Fruitful discussions with C. Wirth, C. Le Quéré, G. Churkina, J. Lloyd, and E.-D. Schulze are gratefully acknowledged. We thank S. Sitch for providing LPJ biosphere model results and S. Körner for the preparation of the meteorological data. We would like to thank the computing centers Gesellschaft für wissenschaftliche Datenverarbeitung Göttingen (Germany) and Deutsches Klimarechenzentrum (Hamburg, Germany) for their kind support. S. H. was supported in part by a grant from the German Ministry for Education and Research (BMBF, 01 LA 9808/9).

## References

- Barford, C. C., Wofsy, S. C., Goulden, M. L., Munger, J. W., Pyle, E. H., Urbanski, S. P., Hutyra, L., Saleska, S. R., Fitzjarrald, D., and Moore, K.: Factors controlling long- and short-term sequestration of atmospheric CO<sub>2</sub> in a mid-latitude forest, *Science*, 294, 1688–1691, 2001. [2577](#)
- Bolin, B. and Keeling, C. D., Large-scale atmospheric mixing as deduced from seasonal and meridional variations of carbon dioxide, *J. Geophys. Res.*, 68, 3899, 1963. [2577](#)
- Bopp, L., Le Quéré, C., Heimann, M., Manning, A., and Monfray, P.: Climate-induced oceanic oxygen fluxes: Implications for the contemporary carbon budget, *Global Biogeochem. Cycles*, 16, No. 0. 10.1029/2001GB001445, 2002. [2605](#), [2632](#)

**CO<sub>2</sub> flux history  
1982–2001**

C. Rödenbeck et al.

Title Page

Abstract

Introduction

Conclusions

References

Tables

Figures

◀

▶

◀

▶

Back

Close

Full Screen / Esc

Print Version

Interactive Discussion

© EGU 2003

Bousquet, P., Peylin, P., Ciais, P., Le Quééré, C., Friedlingstein, P., and Tans, P.: Regional changes in carbon dioxide fluxes of land and oceans since 1980, *Science*, 290, 1342–1346, 2000. [2578](#), [2593](#), [2601](#), [2604](#)

Bruhwieler, L., Tans, P., and Ramonet, M.: A time-dependent assimilation and source retrieval technique for atmospheric tracers, in *Inverse Methods in Global Biogeochemical Cycles*, edited by P. Kasibhatla et al., p. 265, American Geophysical Union, Washington, 2000. [2601](#)

Churkina, G. and Trusilova, K.: A global version of the biome-bgc terrestrial ecosystem model, Tech. Rep., Max Planck Institute for Biogeochemistry, Jena, 2002. [2630](#)

Conway, T., Tans, P., Waterman, L., Thoning, K., Kitzis, D., Masarie, K., and Zhang, N.: Evidence for interannual variability of the carbon cycle from the national oceanic and atmospheric administration climate monitoring and diagnostics laboratory global air sampling network, *J. Geophys. Res.*, 99, 22 831–22 855, 1994. [2578](#), [2583](#), [2585](#), [2590](#), [2597](#), [2598](#)

Dargaville, R., Law, R., and Pribac, F.: Implications of interannual variability in atmospheric circulation on modeled CO<sub>2</sub> concentrations and source estimates, *Global Biogeochemical Cycles*, 14, 931–943, 2000. [2599](#)

DeFries, R. S., Houghton, R. A., Hansen, M. C., Field, C. B., Skole, D., and Townshend, J.: Carbon emissions from tropical deforestation and regrowth based on satellite observations for the 1980s and 1990s, *Proc. Nat. Acad. Sc. USA*, 99, 14 256–14 261, 2002. [2608](#)

Denning, A., Holzer, M., Gurney, K., Heimann, M., Law, R., Rayner, P., Fung, I., Fan, S.-M., Taguchi, S., Friedlingstein, P., Balkanski, Y., Taylor, J., Maiss, M., and Levin, I.: Three-dimensional transport and concentration of sf6. a model intercomparison study (transcom 2), *Tellus B*, 51, 266–297, 1999. [2599](#)

Dentener, F., Feichter, J., and Jeuken, A.: Simulation of the transport of rn222 using on-line and off-line global models at different horizontal resolutions: a detailed comparison with measurements, *Tellus B*, 51, 573–602, 1999. [2599](#)

Falge, E., Baldocchi, D., Tenhunen, J., Aubinet, M., Bakwin, P., Berbigier, P., Bernhofer, C., Burba, G., Clement, R., Davis, K. J., Elbers, J. A., Goldstein, A. H., Grelle, A., Granier, A., Guomundsson, J., Hollinger, D., Kowalski, A. S., Katul, G., Law, B. E., Malhi, Y., Meyers, T., Monson, R. K., Munger, J. W., Oechel, W., Paw, K. T., Pilegaard, K., Rannik, U., Rebmann, C., Suyker, A., Valentini, R., Wilson, K., and Wofsy, S.: Seasonality of ecosystem respiration and gross primary production as derived from FLUXNET measurements, *Agricultural and Forest Meteorology*, 113, 53–74, 2002. [2577](#)

Fan, S., Gloor, M., Mahlmann, J., Pacala, S., Sarmiento, J., Takahashi, T., and Tans, P.: A large

**CO<sub>2</sub> flux history  
1982–2001**

C. Rödenbeck et al.

Title Page

Abstract

Introduction

Conclusions

References

Tables

Figures

◀

▶

◀

▶

Back

Close

Full Screen / Esc

Print Version

Interactive Discussion

© EGU 2003

terrestrial carbon sink in north america implied by atmospheric and oceanic carbon dioxide and models, *Science*, 282, 442, 1998. [2601](#)

5 Feely, R., Waninkhof, R., Takahashi, T., and Tans, P.: Influence of el nino on the equatorial pacific contribution to atmospheric CO<sub>2</sub> accumulation, *Nature*, 398, 597–601, 1999. [2593](#), [2606](#)

Francey, R. J., Tans, P. P., Allison, C. E., Enting, I. G., White, J. W. C., and Trolier, M.: Changes in oceanic and terrestrial carbon uptake since 1982, *Nature*, 373, 326–330, 1995. [2577](#)

Gauss, C. F.: *Theoria combinationis obsevationum erroribus minimis obnoxiae.*, Werke, Vol. 4, 1801. [2580](#)

10 Giering, R. and Kaminski, T.: Recipes for adjoint code construction, *ACM Trans. Math. Software*, 24, 437–474, 1998. [2584](#)

Gloor, M., Gruber, N., Sarmiento, J., Sabine, C., Feely, R., and Rödenbeck, C.: A first estimate of present and preindustrial air-sea CO<sub>2</sub> flux patterns based on ocean interior carbon measurements and models, *Geophys. Res. Lett.*, 30, 10.1029/2002GL015594, 2003. [2594](#), [2606](#), [2628](#), [2630](#)

15 Gurney, K., Law, R. M., Denning, A. S., et al.: Towards robust regional estimates of CO<sub>2</sub> sources and sinks using atmospheric transport models, *Nature*, 415, 626–630, 2002. [2591](#), [2599](#), [2601](#), [2606](#), [2607](#), [2616](#), [2633](#), [2643](#)

Heimann, M.: The global atmospheric transport model TM2, Tech. Rep. 10, Max-Planck-Inst. für Meteorologie, Hamburg, Germany, 1996. [2584](#)

20 Heimann, M. and Keeling, C. D.: A three-dimensional model of atmospheric CO<sub>2</sub> transport based on observed winds, model description and simulated tracer experiments, in *Aspects of Climate Variability in the Pacific and the Western Americas*, edited by D. H. Peterson, vol. 55 of *Geophys. Monogr. Ser.*, pp. 237–275, AGU, Washington, 1989. [2599](#)

25 Houghton, R. A.: Revised estimates of the annual net flux of carbon to the atmosphere from changes in land use and land management 1850–2000, *Tellus*, 55B, 378–390, 2003. [2608](#)

Houweling, S., Rödenbeck, C., Gloor, M., and Heimann, M.: An intercomparison of methods for specifying a priori information in atmospheric CO<sub>2</sub> inversions, in preparation. [2578](#), [2589](#), [2617](#)

30 IPCC: *Climate Change 2001: The Scientific Basis*, Cambridge Univ. Press, Cambridge, 2001. [2592](#), [2616](#), [2628](#), [2632](#)

Jacob, D. J., Prather, M. J., Rasch, P. J., Shia, R. L., Balkanski, Y. J., Beagley, S. R., Bergmann, D. J., Blackshear, W. T., Brown, M., Chiba, M., Chipperfield, M. P., deGrandpre, J., Dignon,

**CO<sub>2</sub> flux history  
1982–2001**

C. Rödenbeck et al.

Title Page

Abstract

Introduction

Conclusions

References

Tables

Figures

◀

▶

◀

▶

Back

Close

Full Screen / Esc

Print Version

Interactive Discussion

© EGU 2003

J. E., Feichter, J., Genthon, C., Grose, W. L., Kasibhatla, P. S., Kohler, I., Kritz, M. A., Law, K., Penner, J. E., Ramonet, M., Reeves, C. E., Rotman, D. A., Stockwell, D. Z., VanVelthoven, P. F. J., Verver, G., Wild, O., Yang, H., and Zimmermann, P.: Evaluation and intercomparison of global atmospheric transport models using rn-222 and other short-lived tracers, *J. Geophys. Res.*, 102, 5953–5970, 1997. [2599](#)

Johnson, E.: Fire and vegetation dynamics Studies from the North American boreal forest. Cambridge Studies in Ecology, Cambridge University Press, New York, 1992. [2611](#)

Kalnay, E. Kanamitsu, M., Kistler, R., et al.: The NCEP/NCAR 40-year reanalysis project, *Bull. Am. Met. Soc.*, 77, 437–471, 1996. [2584](#)

Kaminski, T. and Heimann, M.: Inverse modeling of atmospheric carbon dioxide fluxes, *Science*, 294, 5541,U1–U1, 2001. [2580](#)

Kaminski, T., Rayner, P. J., Heimann, M., and Enting, I. G.: On aggregation errors in atmospheric transport inversions, *J. Geophys. Res.e*, 106, 4703–4715, 2001. [2588](#)

Keeling, C. D., Whorf, T. P., Wahlen, M., and Vanderpligt, J.: Interannual extremes in the rate of rise of atmospheric carbon-dioxide since 1980, *Nature*, 375, 666–670, 1995. [2577](#), [2590](#)

Keeling, R. and Garcia, H.: The change in oceanic oxygen inventory associated with recent global warming, *Proc. National Academy of Sciences*, 99, 7848–7853, 2002. [2605](#), [2632](#)

Keeling, R. and Shertz, S.: Seasonal and interannual variations in atmospheric oxygen and implications for the global carbon cycle, *Nature*, 358, 723–727, 1992. [2605](#)

Kirschbaum, M.: The temperature dependence of soil organic matter decomposition and the effect of global warming on soil organic carbon storage, *Soil Biology and Biochemistry*, 27, 753–760, 1995. [2611](#)

Kurz, W. A. and Apps, M. J.: A 70-year retrospective analysis of carbon fluxes in the canadian forest sector, *Ecological Applications*, 9, 526–547, 1999. [2608](#)

Langenfelds, R. L., Francey, R. J., Pak, B. C., Steele, L. P., Lloyd, J., Trudinger, C. M., and Allison, C. E.: Interannual growth rate variations of atmospheric CO<sub>2</sub> and its  $\delta^{13}\text{C}$ , H<sub>2</sub>, CH<sub>4</sub>, and CO between 1992 and 1999 linked to biomass burning, *Global Biogeochem. Cycles*, 16, doi:10.1029/2001GB001466, 2002. [2615](#)

Larcher, W.: *Oekophysiologie der Pflanzen*, Ulmer Verlag, Stuttgart, 1994. [2611](#)

Law, R. M., Rayner, P. J., Steele, L. P., and Enting, I. G.: Using high temporal frequency data for CO<sub>2</sub> inversions, *Global Biogeochemical Cycles*, 16, 1053, doi:10.1029/2001GB001593, 2002. [2617](#)

Le Quéré, C., Orr, J., Monfray, P., and Aumont, O.: Interannual variability of the oceanic sink of



**CO<sub>2</sub> flux history  
1982–2001**

C. Rödenbeck et al.

Title Page

Abstract

Introduction

Conclusions

References

Tables

Figures

◀

▶

◀

▶

Back

Close

Full Screen / Esc

Print Version

Interactive Discussion

© EGU 2003

- CO<sub>2</sub> from 1979 through 1997, *Global Biogeochemical Cycles*, 14, 1247–1265, 2000. [2593](#)
- Le Quéré, C., Aumont, O., Bousquet, P., Ciais, P., Francey, R., Heimann, M., Keeling, R. F., Kheshti, H., Peylin, P., Piper, S. C., Prentice, I. C., and Rayner, P. J.: Two decades of ocean CO<sub>2</sub> sink and variability, *Tellus*, p. in press, 2003. [2593](#)
- 5 Levitus, S., Antonov, J., Wang, J., Delworth, T., Dixon, K., and Broccoli, A.: Anthropogenic warming of earth's climate system, *Science*, 292, 267–270, 2001. [2605](#)
- Lloyd, J. and Taylor, J. A.: On the temperature dependence of soil respiration, *Functional Ecology*, 8, 315–323, 1994. [2611](#)
- Ludwig, W., Probst, J., and Kempe, S.: Predicting the oceanic input of organic carbon by continental erosion, *Global Biogeochem. Cycles*, 10, 23–41, 1996. [2605](#)
- 10 Maiss, M., Steele, L., Francey, R., Fraser, P., Langenfelds, R., Trivett, N., and Levin, I.: Sulfur hexafluoride – a powerful new atmospheric tracer, *Atmospheric Environment*, 30, 1621–1629, 1996. [2591](#)
- Masarie, K., Langenfelds, R., Allison, C., Conway, T., Dlugokencky, E., Francey, R., Novelli, P., Steele, L., Tans, P., Vaughn, B., and White, J.: NOAA/CSIRO flask air intercomparison experiment: A strategy for directly assessing consistency among atmospheric measurements made by independent laboratories, *J. Geophys. Res.*, 106, 445–464, 2001. [2585](#), [2598](#)
- 15 McGuire, A. Sitch, S., Clein, J. S., et al.: Carbon balance of the terrestrial biosphere in the 20th century: Analysis of CO<sub>2</sub>, climate and land use effects with four process-based ecosystem models, *Global Biogeochemical Cycles*, 15, 183–206, 2001. [2628](#)
- McNeil, B. I., Matear, R. J., Key, R. M., Bullister, J. L., and Sarmiento, J.: Anthropogenic CO<sub>2</sub> uptake by the ocean based on the global chlorofluorocarbon data set, *Science*, 299, 235–239, 2003. [2606](#)
- 20 Nilsson, S. Shvidenko, A., Stolbovoi, V., Gluck, M., Jonas, M., Obersteiner, M.: Full Carbon Account for Russia, International Institute for Applied Systems Analysis, Laxenburg, 2000. [2608](#)
- Olivier, J. G. J. and Berdowski, J. J. M.: Global emissions sources and sinks. In: Berdowski, J., Guicherit, R. and Heij, B. J. (eds.) "The Climate System", A. A. Balkema Publishers/Swets & Zeitlinger Publishers, Lisse, The Netherlands, ISBN 90 5809 255 0, 33–78, 2001. [2628](#)
- 30 Page, S., Siegert, F., Rieley, J. O., Boehm, H. V., Jaya, A., and Limin, S.: The amount of carbon released from peat and forest fires in indonesia during 1997, *Nature*, 420, 61–65, 2002. [2610](#), [2614](#), [2615](#)
- Peylin, P., Baker, D., Sarmiento, J., Ciais, P., and Bousquet, P.: Influence of transport uncer-



**CO<sub>2</sub> flux history  
1982–2001**

C. Rödenbeck et al.

Title Page

Abstract

Introduction

Conclusions

References

Tables

Figures

◀

▶

◀

▶

Back

Close

Full Screen / Esc

Print Version

Interactive Discussion

© EGU 2003

tainty on annual mean and seasonal inversions of atmospheric CO<sub>2</sub> data, J. Geophys. Res., 107, 10.1029/2001JD000857, 2002. [2588](#)

Phillips, O. L., Malhi, Y., Higuchi, N., Laurance, W., Nunez, P., Vasquez, R., Laurance, S. G., Ferreira, L., Stern, M., Brown, S., and Grace, J.: Changes in the carbon balance of tropical forests: Evidence from long-term plots, Science, 282, 439–442, 1998. [2608](#)

Plattner, G.-K., Joos, F., and Stocker, T. F.: Revision of the global carbon budget due to changing air-sea oxygen fluxes, Global Biogeochem. Cycles, 16, art. no. 1096, 2002. [2605](#)  
Press, W., Teukolsky, S., Vetterling, W., and Flannery, B.: Numerical Recipes, Cambridge Univ. Press, 1992. [2582](#)

Rayner, P., Enting, I., Francey, R., and Langenfelds, R.: Reconstructing the recent carbon cycle from atmospheric CO<sub>2</sub>, δCO<sub>2</sub> and O<sub>2</sub>/N<sub>2</sub> observations, Tellus B, 51, 213–232, 1999. [2578](#), [2593](#), [2601](#)

Robock, A.: Pinatubo eruption: The climatic aftermath, Science, 295, 1242–1244, 2002. [2590](#)

Rödenbeck, C., Houweling, S., Gloor, M., and Heimann, M.: Time-dependent atmospheric CO<sub>2</sub> inversions based on interannually varying tracer transport, Tellus B, 55, 488–497, 2003. [2578](#), [2583](#), [2584](#), [2597](#), [2599](#)

Roderick, M. L., Farquhar, G. D., Berry, S. L., and Noble, I. R.: On the direct effect of clouds and atmospheric particles on the productivity and structure of vegetation, Oecologia, 129, 21–30, 2001. [2610](#), [2612](#)

Rustad, L., Campbell, L., Marian, G., Norby, R., Mitchell, M., Hartley, A., Cornelissen, J., and Gurevitch: Gcte-news a meta-analysis of the response of soil respiration, net nitrogen mineralisation, and above-ground plant growth to experimental warming, Oecologia, 126, 543–562, 2001. [2610](#)

Sarmiento, J. and Sundquist, E.: Revised budget for the oceanic uptake of anthropogenic carbon dioxide, Nature, 356, 589–593, 1992. [2605](#)

Schulze, E.-D., (ed.): Carbon and Nitrogen Cycling in European Forest Ecosystems, Springer, Berlin, Heidelberg, New York, 2000. [2577](#)

Serreze, M. C., Walsh, J. E., Chapin III, F. S., Osterkamp, T., Dyurgerov, M., Romanovsky, V., Oechel, W. C., Morison, J., Zhang, T., and Barry, R. G.: Observational Evidence of recent change in the northern high-latitude environment, Climatic Change, 46, 159–207, 2000. [2608](#)

Shvidenko, A. and Nilsson, S.: A synthesis of the impact of russian forests on the global carbon budget for 1961–1998, Tellus B, 55, 391–415, 2003. [2608](#)

**CO<sub>2</sub> flux history  
1982–2001**

C. Rödenbeck et al.

Title Page

Abstract

Introduction

Conclusions

References

Tables

Figures

◀

▶

◀

▶

Back

Close

Full Screen / Esc

Print Version

Interactive Discussion

© EGU 2003

Sitch, S., Prentice, I., Smith, B., Cramer, W., Kaplan, J., Lucht, W., Sykes, M.; Thonicke, K., and Venevsky, S.: LPJ – a coupled model of vegaetation dynamics and the terrestrial carbon cycle, in "The role of vegetation dynamics in the control of atmospheric CO<sub>2</sub> content" (S. Sitch, PhD Thesis), Lund University, Lund (Sweden), 2000. [2628](#), [2630](#)

5 Takahashi, T.: Global sea-air CO<sub>2</sub> flux based on climatological surface ocean pCO<sub>2</sub> and seasonal biological and temperature effects, Deep Sea Res. II, 49, 1601–1622, 2002. [2606](#), [2633](#)

Takahashi, T. Wanninkhof, R. H., Feely, R. A., et al.: Net sea-air CO<sub>2</sub> flux over the global oceans: An improved estimate based on the sea-air pCO<sub>2</sub> difference, Proc. 2nd CO<sub>2</sub> in Oceans Symposium (Tsukuba, Japan), 1999. [2577](#), [2594](#), [2606](#), [2628](#), [2630](#)

10 Tarantola, A.: Inverse Problem Theory, Methods for Data Fitting and Model Parameter Estimation, Elsevier, New York, 1987. [2582](#), [2589](#), [2602](#)

Tian, H., Melillo, J. M., Kicklighter, D. W., McGuire, A. D., Helfrich III, J. V. K., Moore III, B., and Vörösmarty, C. J.: Effect of interannual climate variability on carbon storage in Amazonian ecosystems, Nature, 396, 664–667, 1998. [2614](#)

15 Wanninkhof, R.: Relationship between wind speed and gas exchange, J. Geophys. Res., 97, 7373–7382, 1992. [2628](#), [2633](#)

Wolter, K. and Timlin, M.: Monitoring ENSO and COADS with a seasonally adjusted principal component index, in Proc. of the 17th Climate Diagnostics Workshop, Norman, OK, 52–57, NOAA/N MC/CAC, NSSL, Oklahoma Clim. Survey, CIMMS and the School of Meteor., Univ. of Oklahoma, 1993. [2638](#)

20 Zhou, L., Tucker, C. J., Kaufmann, R. K., Slayback, D., Shabanov, N. V., and Myneni, R. B.: Variations in northern vegetation activity inferred from atellite data of vegetation index during 1981 to 1999, J. Geophys. Res., 106, 20,069–20,083, 2001. [2608](#)

**Table 1.** Stations measuring CO<sub>2</sub> concentrations that were used in the inversion. The symbols refer to Fig. 1. (to be continued on next page)

Code	Name	Latitude (°)	Longitude (°)	Height (m a.s.l.)
▲ asc	Ascension Island	-7.92	-14.42	54
▲ brw	Barrow, Alaska	71.32	-156.60	11
▲ gmi	Guam, Mariana Island	13.43	144.78	2
▲ key	Key Biscayne, Florida	25.67	-80.20	3
▲ kum	Cape Kumukahi, Hawaii	19.52	-154.82	3
▲ mlo	Mauna Loa, Hawaii	19.53	-155.58	3397
▲ nwr	Niwot Ridge	40.05	-105.58	3475
▲ psa	Palmer Station, Antarctica	-64.92	-64.00	10
▲ smo	Tutuila, American Samoa	-14.25	-170.57	42
▲ spo	South Pole	-89.98	-24.80	2810
▲ stm	Station 'M'	66.00	2.00	7
◆ alt	Alert	82.45	-62.52	210
◆ cgo	Cape Grim, Tasmania	-40.68	144.68	94
◆ mid	Sand Island, Midway	28.22	-177.37	4
◆ sey	Mahe Island, Seychelles	-4.67	55.17	3
◆ shm	Shemya Island, Alaska	52.72	174.10	40
■ bme	St. David's Head, Bermuda	32.37	-64.65	30
■ bmw	Southampton, Bermuda	32.27	-64.88	30
■ rpb	Ragged Point, Barbados	13.17	-59.43	3
■ bal	Baltic Sea, Poland	55.50	16.67	7
■ hun	Hegyhatsal, Hungary	46.95	16.65	344
■ ice	Heimaey, Iceland	63.25	-20.15	100
■ izo	Izaña, Tenerife	28.30	-16.48	2360
■ mhd	Mace Head, Ireland	53.33	-9.90	25
■ tap	Tae-ahn Peninsula, Korea	36.73	126.13	20
■ uum	Ulaan Uul, Mongolia	44.45	111.10	914

## CO<sub>2</sub> flux history 1982–2001

C. Rödenbeck et al.

Title Page

Abstract

Introduction

Conclusions

References

Tables

Figures

◀

▶

◀

▶

Back

Close

Full Screen / Esc

Print Version

Interactive Discussion

© EGU 2003

## CO<sub>2</sub> flux history 1982–2001

C. Rödenbeck et al.

Table 1. Continued

Code	Name	Latitude (°)	Longitude (°)	Height (m a.s.l.)
★ ask	Assekrem, Algeria	23.18	5.42	2728
★ azr	Terceira Island, Azores	38.75	-27.08	30
★ bsc	Black Sea, Constanta, Romania	44.17	28.68	3
★ eic	Easter Island	-29.15	-109.43	50
★ hba	Halley Bay, Antarctica	-75.67	-25.50	10
★ lef	Park Falls, Wisconsin	45.93	-90.27	868
★ tdf	Tierra del Fuego	-54.87	-68.48	20
★ uta	Wendover, Utah	39.90	-113.72	1320
★ zep	Zeppelin, Spitsbergen	78.90	11.88	474
● cba	Cold Bay, Alaska	55.20	-162.72	25
● chr	Christmas Island	1.70	-157.17	3
● cmo	Cape Meares, Oregon	45.48	-123.97	30
● crz	Crozet	-46.45	51.85	120
● itn	Grifton, North Carolina	35.35	-77.38	505
● mbc	Mould Bay, Canada	76.25	-119.35	58
● wlg	Mt. Waliguan, China	36.27	100.92	3810

[Title Page](#)
[Abstract](#)
[Introduction](#)
[Conclusions](#)
[References](#)
[Tables](#)
[Figures](#)
[◀](#)
[▶](#)
[◀](#)
[▶](#)
[Back](#)
[Close](#)
[Full Screen / Esc](#)
[Print Version](#)
[Interactive Discussion](#)

## CO<sub>2</sub> flux history 1982–2001

C. Rödenbeck et al.

**Table 2.** Specification of the different inversion runs. In the text, they are referred to by their respective number of stations

# of stations	Station sets used	Target period
11	▲	01/1982–12/2000
16	▲+◆	01/1986–12/2000
19	▲+◆+■	01/1990–12/2000
26	▲+◆+■+■	01/1993–12/2000
35	▲+◆+■+■+★	01/1996–12/2000
42	▲+◆+■+■+★+●	(inhomogeneous)

[Title Page](#)
[Abstract](#)
[Introduction](#)
[Conclusions](#)
[References](#)
[Tables](#)
[Figures](#)
[|◀](#)
[▶|](#)
[◀](#)
[▶](#)
[Back](#)
[Close](#)
[Full Screen / Esc](#)
[Print Version](#)
[Interactive Discussion](#)

CO<sub>2</sub> flux history  
1982–2001

C. Rödenbeck et al.

Title Page

Abstract

Introduction

Conclusions

References

Tables

Figures

◀

▶

◀

▶

Back

Close

Full Screen / Esc

Print Version

Interactive Discussion

© EGU 2003

**Table 3.** Sources of information for the a-priori fluxes and the flux model used in the standard inversion set-up

	Fossil fuel	Land biosphere NEE	Ocean
<b>Interannual?</b>	yes	no	no
<b>Seasonal?</b>	no	yes	yes
<b>Flux</b>	Yearly totals according to global statistics from the EDGAR data base (Olivier et al., 2001). Geographical distribution according to EDGAR's emission fields for 1990 or 1995, respectively, with linear interpolation in between.	Mean seasonal cycle of NEE over 1980–1992 as estimated by a simulation with the LPJ biosphere model (Sitch et al., 2000).	Large-scale long-term fluxes as estimated by an inversion based on ocean carbon data (Gloor et al., 2003). Small-scale spatial patterns and seasonal cycle proportional to the exchange fluxes by Takahashi et al. (1999) based on CO <sub>2</sub> partial pressure difference across the air-sea interface and a gas exchange coefficient depending quadratically on mean wind speed (Wanninkhof, 1992).
<b>Global uncertainty</b>	0.37 PgC/yr (corresponding to 6% relative uncertainty, IPCC (2001)) with respect to a 10 year average.	0.85 PgC/yr (standard deviation between the 4 terrestrial biosphere models that took part in the CCMLP intercomparison, McGuire et al. (2001)) with respect to a 10 year average.	0.5 PgC/yr (IPCC, 2001) with respect to a 4 year average.

---

**CO<sub>2</sub> flux history  
1982–2001**

C. Rödenbeck et al.

---

[Title Page](#)
[Abstract](#)[Introduction](#)[Conclusions](#)[References](#)[Tables](#)[Figures](#)[◀](#)[▶](#)[◀](#)[▶](#)[Back](#)[Close](#)[Full Screen / Esc](#)[Print Version](#)[Interactive Discussion](#)

© EGU 2003

**Table 3.** Continued

	<b>Fossil fuel</b>	<b>Land biosphere NEE</b>	<b>Ocean</b>
<b>Flux model shape</b>	-/-	Proportional to the long-term mean (1980–1992) of NPP as modelled by LPJ. No seasonal or inter-annual dependence.	No structure in space or time (proportional to grid cell area and time interval).
<b>Spatial correlation</b>	scale $1R \approx 6375$ km	scale $0.2R \approx 1275$ km	scale $0.3R \approx 1912$ km

## CO<sub>2</sub> flux history 1982–2001

C. Rödenbeck et al.

**Table 4.** Specification of the set-up changes taken for the individual sensitivity inversions. For more details see Sect. 2.2. The last column gives normalized a-posteriori concentration mismatch per degree of freedom, as a measure how well the concentration data were fitted (35 stations case)

Code	Specification (standard set up)	$\chi_c^2/n$ 0.82
(a)	A-priori ocean-atmosphere exchange flux according to <a href="#">Takahashi et al. (1999)</a> in place of <a href="#">Gloor et al. (2003)</a> .	0.81
(b)	Fluxes inferred for 39 large uncorrelated inversion regions rather than 730 spatially correlated grid scale regions.	0.98
(c)	Homogeneous geographical distribution of the land flux update, rather than in proportion to an yearly NPP estimate.	0.78
(d)	A-priori correlation in time on a 2 months scale (with complete decay after 4 months), rather than uncorrelated months.	1.32
(e)	A-priori land-atmosphere exchange flux according to <a href="#">Churkina and Trusilova (2002)</a> in place of <a href="#">Sitch et al. (2000)</a> .	0.79
(f)	Global a-priori ocean uncertainty 1 PgC/yr instead of 0.5 PgC/yr.	0.69

[Title Page](#)
[Abstract](#)
[Introduction](#)
[Conclusions](#)
[References](#)
[Tables](#)
[Figures](#)
[Back](#)
[Close](#)
[Full Screen / Esc](#)
[Print Version](#)
[Interactive Discussion](#)



## CO<sub>2</sub> flux history 1982–2001

C. Rödenbeck et al.

[Title Page](#)
[Abstract](#)
[Introduction](#)
[Conclusions](#)
[References](#)
[Tables](#)
[Figures](#)
[Back](#)
[Close](#)
[Full Screen / Esc](#)
[Print Version](#)
[Interactive Discussion](#)

© EGU 2003

**Table 5.** Important examples of features that entirely depend on individual stations, disappearing as soon as that station is removed from the set. Smaller features or smaller time-mean shifts, as well as changes in amplitude of temporal features (indicating that these features are also supported by other stations), are not listed here. Implications for the robustness of these features are discussed in Sect. 4.1

Station	Feature
ASC	Drop by $\approx 1$ PgC/yr in 1989 in ‘Southern Africa’ (Fig. 5, part IV)
GMI	Sharp increase in 1985 and sharp decrease in 1992 in ‘West Pacific Tropics’ and ‘North Pacific Tropics’ (Fig. 5, part V) and, consequently, the ocean total (part II)
KEY	Large increases in ‘American Boral’, ‘American Temp.’ end of 2001, corresponding decreases in ‘Eurasian Boral’, ‘Eurasian Temperate’, and ‘Europe’ (Fig. 5, part IV)
SMO	Long-term trends and time-mean values in ‘South American Trop.’ (Fig. 5, part IV) and many ocean regions (part V)
SEY	almost all time variability in ‘Indian Tropical Ocean’ and ‘S Indian Temp. Ocean’ (Fig. 5, part V; see case of 11 stations that does not contain SEY), similarly in ‘Tropical Asia’ (part IV)
BME	negative peaks in ‘North American Bor.’ and ‘North American Temp.’ around 1993
BSC	long-term fluxes: large outgassing in ‘Europe’ (35 stations case in Figs. 5 [part IV], 7, 8)
EIC	long-term fluxes: large uptake in ‘South Pacific Temp.’ (35 stations case in Figs. 5 [part V], 7, 8)
HBA	long-term fluxes: shifts between ‘South American Temp.’, ‘South Atlantic Temp.’, and ‘Southern Ocean’ (35 stations case in Figs. 5 [parts IV and V])

CO<sub>2</sub> flux history  
1982–2001

C. Rödenbeck et al.

**Table 6.** Global ocean and land carbon exchange (PgC/yr). The fossil fuel component (as given by the a-priori assumption) has been subtracted. Positive values denote a net source of non-fossil fluxes into the atmosphere. Given  $\pm 1\sigma$  intervals for the inversion results represent the statistical a-posteriori uncertainty only

	Land-Atmosphere flux	Ocean-Atmosphere flux	Total
<b>01/1980–12/1989</b>			
11 stations <sup>a</sup>	-1.1 ± 0.3	-1.2 ± 0.3	-2.2 ± 0.1
Bopp et al. (2002)	-0.9* (-0.3 ± 0.9)	-1.2* (-1.8 ± 0.8)	-2.1
IPCC (2001)	-0.8* (-0.2 ± 0.7)	-1.3* (-1.9 ± 0.6)	-2.1 <sup>b</sup>
<b>01/1990–12/1999</b>			
11 stations	-1.8 ± 0.3	-1.4 ± 0.3	-3.3 ± 0.1
16 stations	-1.6 ± 0.3	-1.7 ± 0.2	-3.3 ± 0.1
Keeling and Garcia (2002)	-1.9* (-1.3 ± 0.8)	-1.3* (-1.9 ± 0.6)	-3.1 ± 0.3
IPCC, 2001	-2.0* (-1.4 ± 0.7)	-1.1* (-1.7 ± 0.5)	-3.1 <sup>b</sup>
<b>01/1990–12/1996</b>			
11 stations	-2.1 ± 0.3	-1.4 ± 0.3	-3.5 ± 0.1
16 stations	-2.0 ± 0.3	-1.6 ± 0.3	-3.6 ± 0.1
Bopp et al. (2002)	-1.8* (-1.2 ± 0.9)	-1.7* (-2.3 ± 0.7)	-3.5
<b>01/1996–12/1999</b>			
11 stations	-1.5 ± 0.4	-1.5 ± 0.4	-3.0 ± 0.2
16 stations	-1.2 ± 0.4	-1.7 ± 0.4	-2.9 ± 0.2
26 stations	-1.1 ± 0.4	-1.8 ± 0.4	-2.9 ± 0.1
35 stations	-1.2 ± 0.4	-1.7 ± 0.4	-2.9 ± 0.1

\* Assuming a riverine land-ocean carbon transport of 0.8 PgC yr<sup>-1</sup> of which 0.2 PgC yr<sup>-1</sup> are buried in ocean sediments. Original numbers in parentheses.

<sup>a</sup> Actual time span only 01/1982–12/1989.

<sup>b</sup> Sum of the previous two columns.

Title Page

Abstract

Introduction

Conclusions

References

Tables

Figures

◀

▶

◀

▶

Back

Close

Full Screen / Esc

Print Version

Interactive Discussion

**Table 7.** Carbon exchange resolved into Northern hemisphere, tropics and the Southern hemisphere (PgC/yr). Conventions as in Table 6

	Time span	S hemisphere ( $\leq -20^\circ$ )	Tropics	N hemisphere ( $\geq 20^\circ$ )	Total
<b>Land</b>					
16 stations	01/1992–12/1996	$-0.1 \pm 0.2$	$-1.2 \pm 0.3$	$-0.5 \pm 0.2$	$-1.8 \pm 0.4$
26 stations	"	$-0.0 \pm 0.2$	$-1.0 \pm 0.3$	$-0.7 \pm 0.2$	$-1.8 \pm 0.4$
35 stations	01/1996–12/1999	$0.1 \pm 0.2$	$-0.8 \pm 0.4$	$-0.4 \pm 0.2$	$-1.2 \pm 0.4$
a-priori		$-0.1 \pm 0.2$	$0.3 \pm 0.9$	$-0.8 \pm 1.0$	$-0.5 \pm 1.5$
Gurney et al. (2002)	01/1992–12/1996	$0.0 \pm 1.1$	$1.0 \pm 1.3$	$-2.2 \pm 0.7$	-1.2
<b>Ocean</b>					
16 stations	01/1992–12/1996	$-1.0 \pm 0.1$	$0.9 \pm 0.2$	$-1.6 \pm 0.2$	$-1.7 \pm 0.3$
26 stations	"	$-1.0 \pm 0.1$	$0.9 \pm 0.2$	$-1.6 \pm 0.1$	$-1.7 \pm 0.3$
35 stations	01/1996–12/1999	$-1.2 \pm 0.2$	$1.1 \pm 0.2$	$-1.7 \pm 0.1$	$-1.7 \pm 0.4$
a-priori		$-1.8 \pm 0.3$	$1.4 \pm 0.2$	$-1.4 \pm 0.2$	$-1.8 \pm 0.5$
Takahashi (2002)*	1995	-1.5	0.8	-1.1	-1.8
Takahashi (2002)**	1995	-1.4	0.5	-1.2	-2.0
Gurney et al. (2002)	01/1992–12/1996	$-0.9 \pm 0.7$	$0.5 \pm 0.6$	$-1.1 \pm 0.4$	-1.5
<b>Global</b>					
16 stations	01/1992–12/1996	-1.1	-0.3	-2.1	$-3.5 \pm 0.1$
26 stations	"	-1.0	-0.1	-2.3	$-3.5 \pm 0.1$
35 stations	01/1996–12/1999	-1.1	0.3	-2.1	$-2.9 \pm 0.1$
a-priori		-1.9	1.7	-2.2	$-2.3 \pm 1.6$
Gurney et al. (2002)	01/1992–12/1996	-0.9	0.7	-3.3	-3.1

\* Using parameterization of gas exchange velocity based on the square of wind speed of Wanninkhof (1992)

\*\* Using parameterization of gas exchange velocity based on the third power of wind speed of Wanninkhof (1992)

## CO<sub>2</sub> flux history 1982–2001

C. Rödenbeck et al.

Title Page

Abstract

Introduction

Conclusions

References

Tables

Figures

◀

▶

◀

▶

Back

Close

Full Screen / Esc

Print Version

Interactive Discussion

**CO<sub>2</sub> flux history  
1982–2001**

C. Rödenbeck et al.

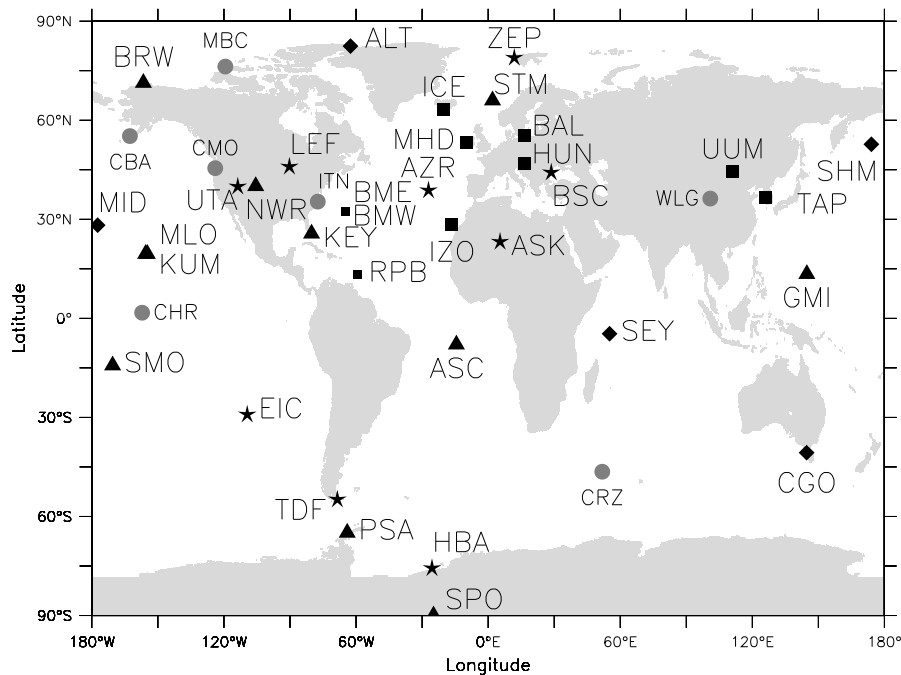


**Fig. 1.** Location of the atmospheric measurement stations used in the inversion (cf. Table 1). The different symbols group the stations into sets with differently long records (see Table 2 and Fig. 2).

[Title Page](#)[Abstract](#)[Introduction](#)[Conclusions](#)[References](#)[Tables](#)[Figures](#)[◀](#)[▶](#)[◀](#)[▶](#)[Back](#)[Close](#)[Full Screen / Esc](#)[Print Version](#)[Interactive Discussion](#)

© EGU 2003

## CO<sub>2</sub> flux history 1982–2001

C. Rödenbeck et al.

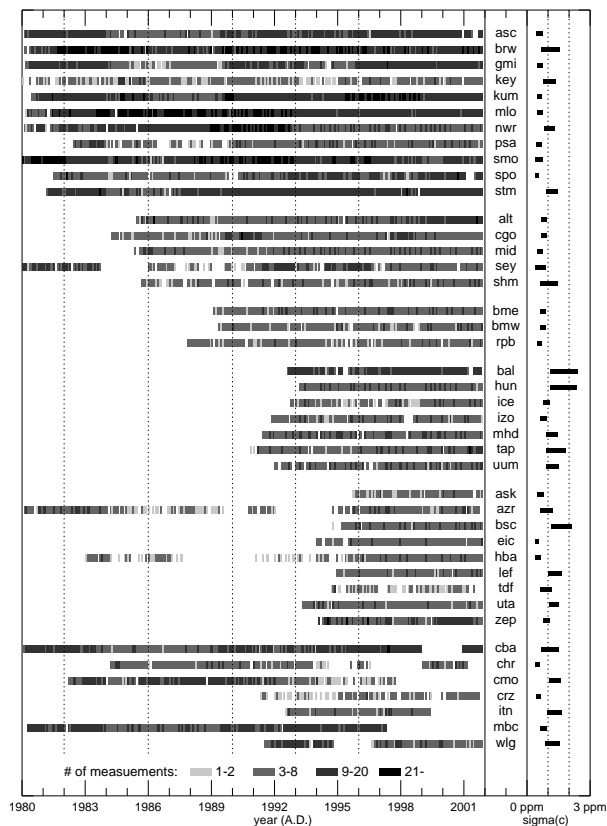


**Fig. 2.** Left: Availability of CO<sub>2</sub> concentration data at the individual stations (number of valid flasks). Right: Range of uncertainty intervals (comprising both measurement uncertainty and model representation error) used in the inversion.

[Title Page](#)
[Abstract](#)
[Introduction](#)
[Conclusions](#)
[References](#)
[Tables](#)
[Figures](#)
[◀](#)
[▶](#)
[◀](#)
[▶](#)
[Back](#)
[Close](#)
[Full Screen / Esc](#)
[Print Version](#)
[Interactive Discussion](#)

**CO<sub>2</sub> flux history  
1982–2001**

C. Rödenbeck et al.

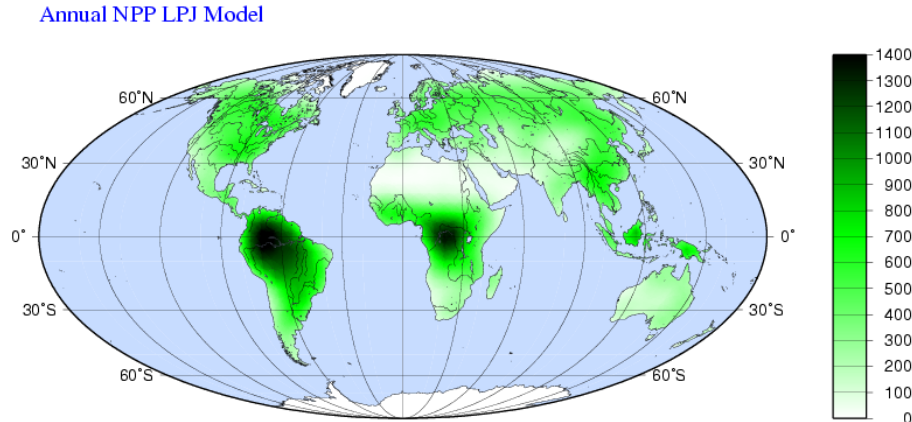


**Fig. 3.** Spatial pattern shaping those flux adjustments of the inversion that refer to the terrestrial biosphere. The exact meaning is explained in Sect. 2.2.4. The pattern (arbitrary units) is proportional to an estimate of annual NPP.

[Title Page](#)[Abstract](#)[Introduction](#)[Conclusions](#)[References](#)[Tables](#)[Figures](#)[◀](#)[▶](#)[◀](#)[▶](#)[Back](#)[Close](#)[Full Screen / Esc](#)[Print Version](#)[Interactive Discussion](#)

© EGU 2003

**CO<sub>2</sub> flux history  
1982–2001**

C. Rödenbeck et al.

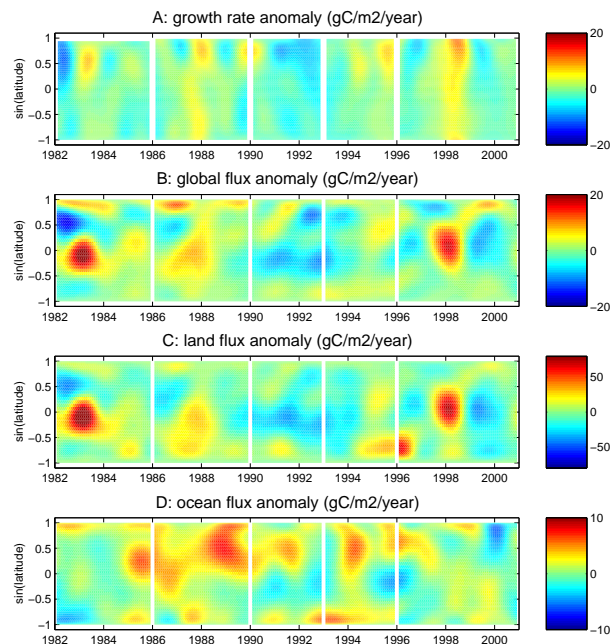


**Fig. 4.** (A) Atmospheric CO<sub>2</sub> growth rate anomalies as measured at the stations (linearly interpolated between the stations; units converted to an equivalent CO<sub>2</sub> flux into a well-mixed column). (B) Surface CO<sub>2</sub> flux anomalies as estimated by the inversion. (C) As B, but land fluxes only. (D) As B, but ocean fluxes only. - In all panels, quantities are averaged over longitude, and deseasonalized by running yearly averaging. Further, they are smoothed with a 4th order Butterworth filter with frequencies  $1/(7 \text{ month})$  in time and approximately  $1/(20^\circ)$  in latitude. The five sections in time (delimited by the white gaps in 1986, 1990, 1993, and 1996) are based on 11, 16, 19, 26, and 35 stations, respectively (see Table 1), where anomalies are formed by subtracting the respective time averages of the identical period 01/1996–12/2000. The different ranges of the colour scales in the panels indicate different amplitudes of the anomalies.

[Title Page](#)[Abstract](#)[Introduction](#)[Conclusions](#)[References](#)[Tables](#)[Figures](#)[◀](#)[▶](#)[◀](#)[▶](#)[Back](#)[Close](#)[Full Screen / Esc](#)[Print Version](#)[Interactive Discussion](#)

© EGU 2003

CO<sub>2</sub> flux history  
1982–2001

C. Rödenbeck et al.

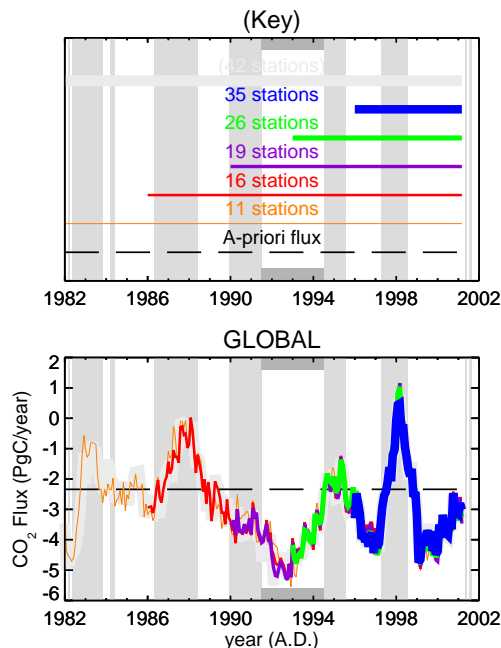


**Fig. 5.** Part I: Time series of the global surface CO<sub>2</sub> flux as estimated by our inversion (standard set-up). The fossil fuel component (as given by the a-priori assumption) has been subtracted. Positive values denote a net source of non-fossil fluxes into the atmosphere. Fluxes are deseasonalized by summing over running yearly intervals. The five solid color lines correspond to inversions with differently large station sets (Table 2). They extend only over those time intervals in which all participating data records fulfill our requirement of high homogeneity in time (see Sect. 2.2.1). The light grey curve denotes the case with maximal 42 stations, where the number of actually available stations strongly changes in time. The dashed line denotes the a-priori flux values. The background stripes in each panel indicate a classification of the months into ‘El Niño’ (grey) or ‘La Niña’ (white) periods (values of the MOI index (Wolter and Timlin, 1993) above or below 0.05, respectively), except for a ‘Post-Pinatubo’ period (dark gray horizontal bars).

Title Page

Abstract

Introduction

Conclusions

References

Tables

Figures

◀

▶

◀

▶

Back

Close

Full Screen / Esc

Print Version

Interactive Discussion



**CO<sub>2</sub> flux history  
1982–2001**

C. Rödenbeck et al.

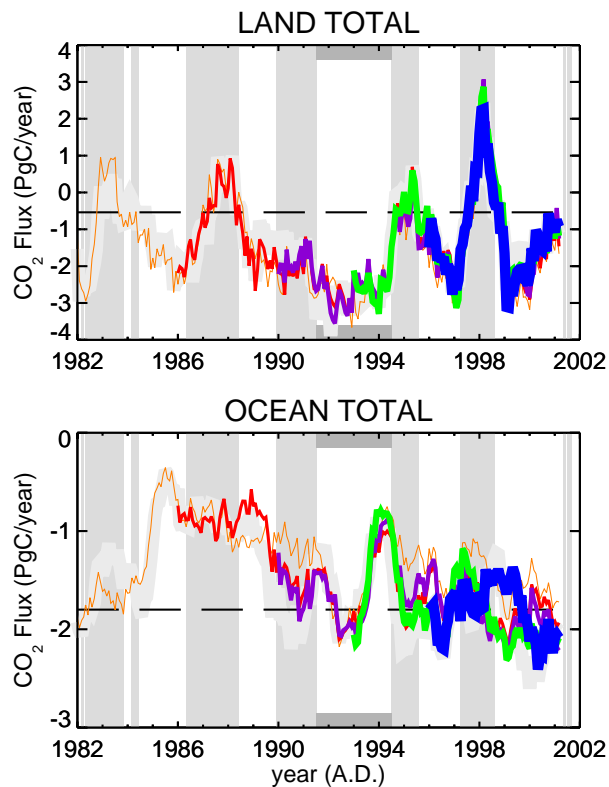


**Fig. 5.** Continued. Part II: Breakup of the standard estimates into land-atmosphere and ocean-atmosphere fluxes.

[Title Page](#)[Abstract](#)[Introduction](#)[Conclusions](#)[References](#)[Tables](#)[Figures](#)[◀](#)[▶](#)[◀](#)[▶](#)[Back](#)[Close](#)[Full Screen / Esc](#)[Print Version](#)[Interactive Discussion](#)

© EGU 2003

## CO<sub>2</sub> flux history 1982–2001

C. Rödenbeck et al.

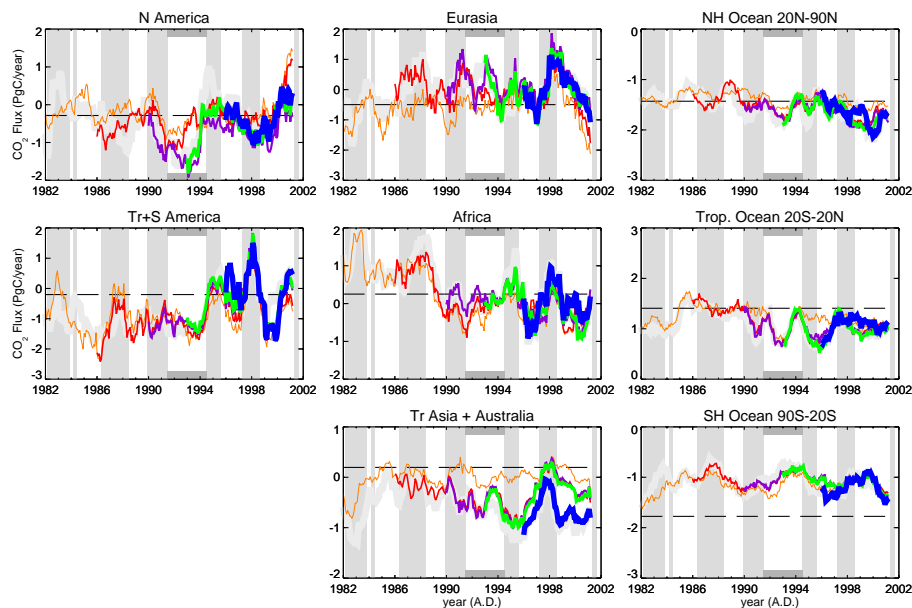


**Fig. 5.** Continued. Part III: Breakup of the estimated land-atmosphere fluxes into 5 ‘continents’ (left and middle column), and the ocean-atmosphere fluxes into 3 latitudinal bands (right column). For a map of the regions see Fig. 6.

[Title Page](#)
[Abstract](#)
[Introduction](#)
[Conclusions](#)
[References](#)
[Tables](#)
[Figures](#)
[◀](#)
[▶](#)
[◀](#)
[▶](#)
[Back](#)
[Close](#)
[Full Screen / Esc](#)
[Print Version](#)
[Interactive Discussion](#)

## CO<sub>2</sub> flux history 1982–2001

C. Rödenbeck et al.

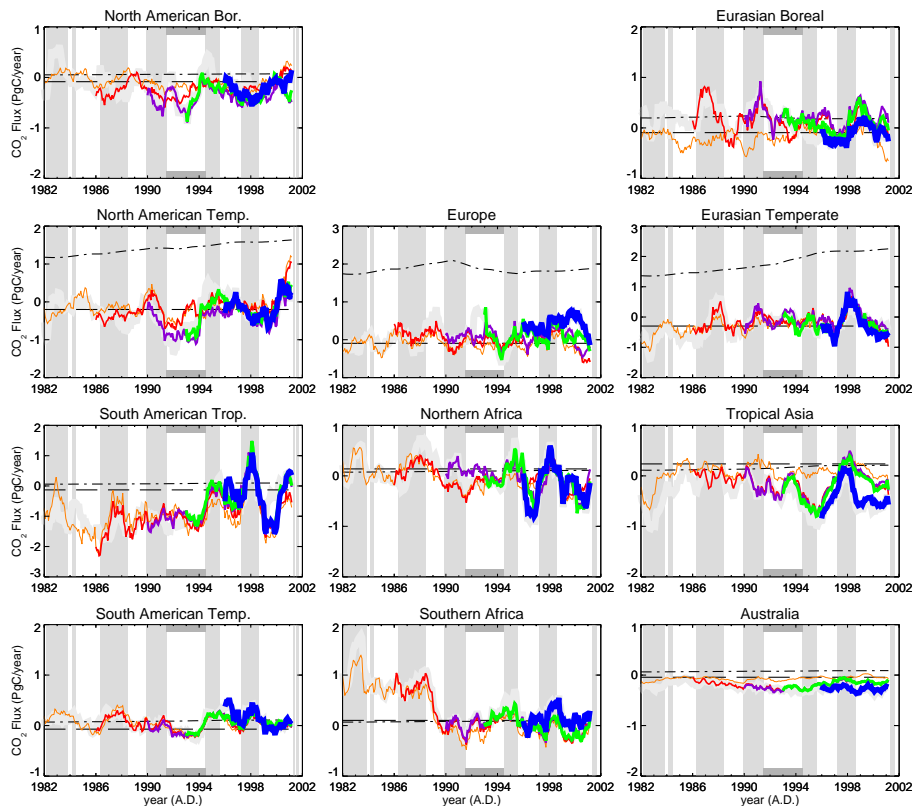


**Fig. 5.** Continued. Part IV: Breakup of the standard flux estimates into the 11 land regions of TransCom3. For a map of the regions see Fig. 6. As an additional information, the a-priori assumed fossil fuel component is shown here as a dash-dotted black line.

[Title Page](#)
[Abstract](#)
[Introduction](#)
[Conclusions](#)
[References](#)
[Tables](#)
[Figures](#)
[◀](#)
[▶](#)
[◀](#)
[▶](#)
[Back](#)
[Close](#)
[Full Screen / Esc](#)
[Print Version](#)
[Interactive Discussion](#)

CO<sub>2</sub> flux history  
1982–2001

C. Rödenbeck et al.

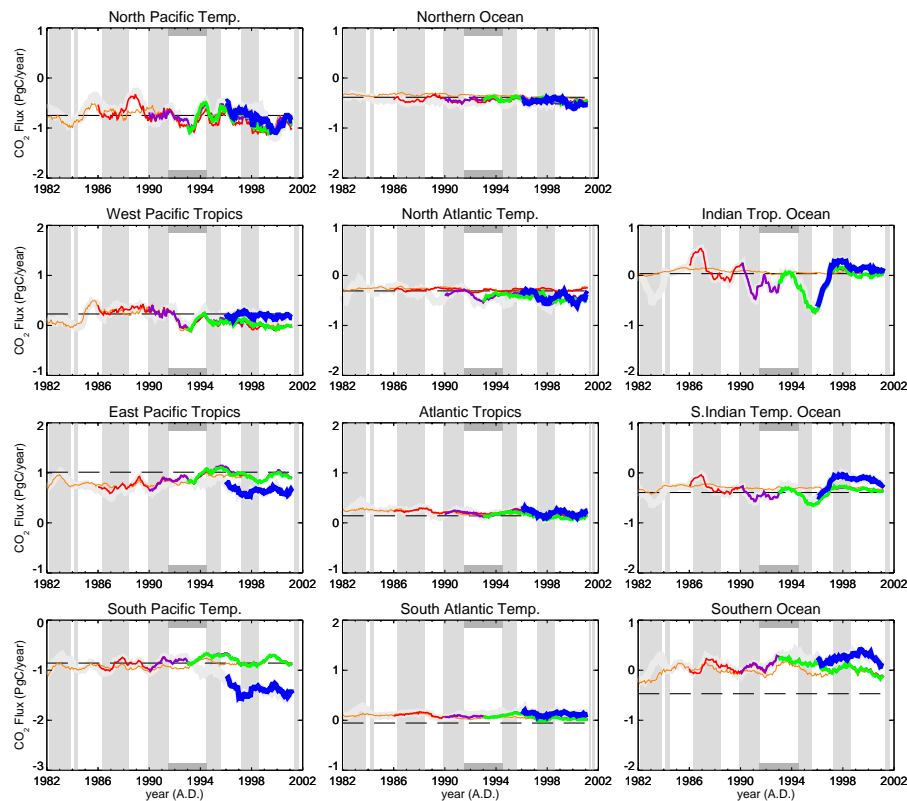


**Fig. 5.** Continued. Part V: Breakup of the standard flux estimates into the 11 ocean regions of TransCom3. For a map of the regions see Fig. 6.

[Title Page](#)[Abstract](#)[Introduction](#)[Conclusions](#)[References](#)[Tables](#)[Figures](#)[◀](#)[▶](#)[◀](#)[▶](#)[Back](#)[Close](#)[Full Screen / Esc](#)[Print Version](#)[Interactive Discussion](#)

© EGU 2003

CO<sub>2</sub> flux history  
1982–2001

C. Rödenbeck et al.

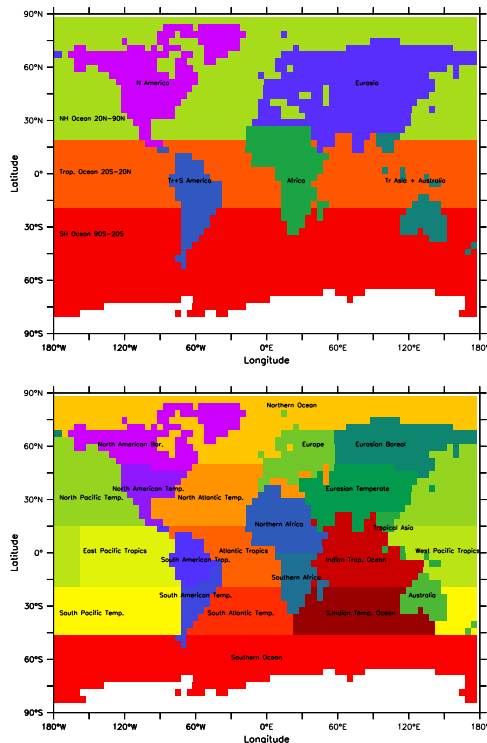


**Fig. 6.** Maps of the regions over which the estimated fluxes are integrated to obtain different parts of Figs. 5, 7, 9, and 10. Upper panel: Continental scale regions used in parts III of the time series figures and second panels of the bar figures. Lower panel: Regions as defined in the TransCom3 project (Gurney et al., 2002), used in parts IV and V of the time series figures and third and fourth panels of the bar figures. Note that neighbouring land and ocean regions actually overlap each other beyond the coast line, with the integration of fluxes being done over the land and ocean component, respectively, only. The apparent coast lines shown here correspond to a land/water map at the resolution of the transport model.

Title Page

Abstract

Introduction

Conclusions

References

Tables

Figures

◀

▶

◀

▶

Back

Close

Full Screen / Esc

Print Version

Interactive Discussion

CO<sub>2</sub> flux history  
1982–2001

C. Rödenbeck et al.

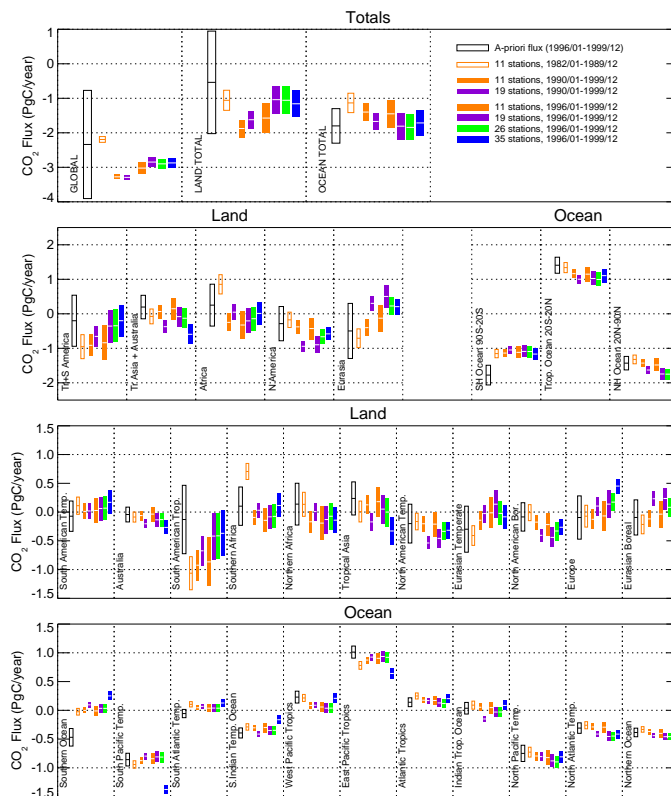


**Fig. 7.** Long-term averages of yearly fluxes from the standard inversion. Different bar widths/signatures refer to different averaging periods ('Eighties', 'Nineties', and 'Late nineties'), while different colours refer to the different runs (based on 11, 19, 26, or 35 stations). From the top to the bottom panel, the spatial scale of integration is more and more refined, as for parts I through V of Fig. 5. The lengths of the bars give the a-posteriori  $\pm 1\sigma$  intervals (with respect to the averages). The best-guess values themselves are highlighted as central white lines.

Title Page

Abstract

Introduction

Conclusions

References

Tables

Figures

◀

▶

◀

▶

Back

Close

Full Screen / Esc

Print Version

Interactive Discussion

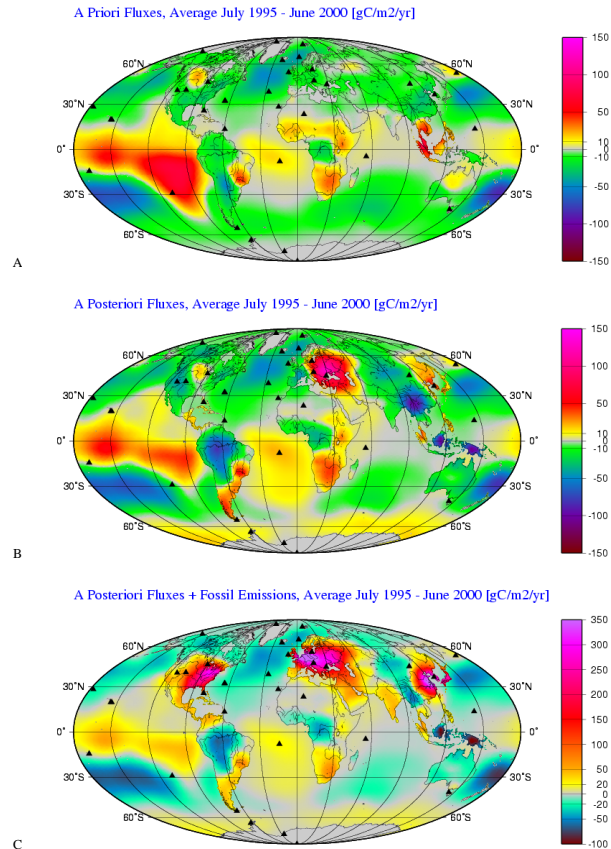


**Fig. 8.** Mean flux estimates (07/1995–06/2000) as global maps. **(A)** A-priori flux field (without fossil fuel component). **(B)** A-posteriori flux field estimated using 35 stations (without fossil fuel component). **(C)** Total a-posteriori flux field, including fossil fuel emissions. Fluxes are shown at the resolution of the transport model (about 4° latitude × 5° longitude). The continental outlines separate the land and ocean fluxes that are treated as separate components in the calculation.

[Title Page](#)
[Abstract](#)
[Introduction](#)
[Conclusions](#)
[References](#)
[Tables](#)
[Figures](#)
[◀](#)
[▶](#)
[◀](#)
[▶](#)
[Back](#)
[Close](#)
[Full Screen / Esc](#)
[Print Version](#)
[Interactive Discussion](#)

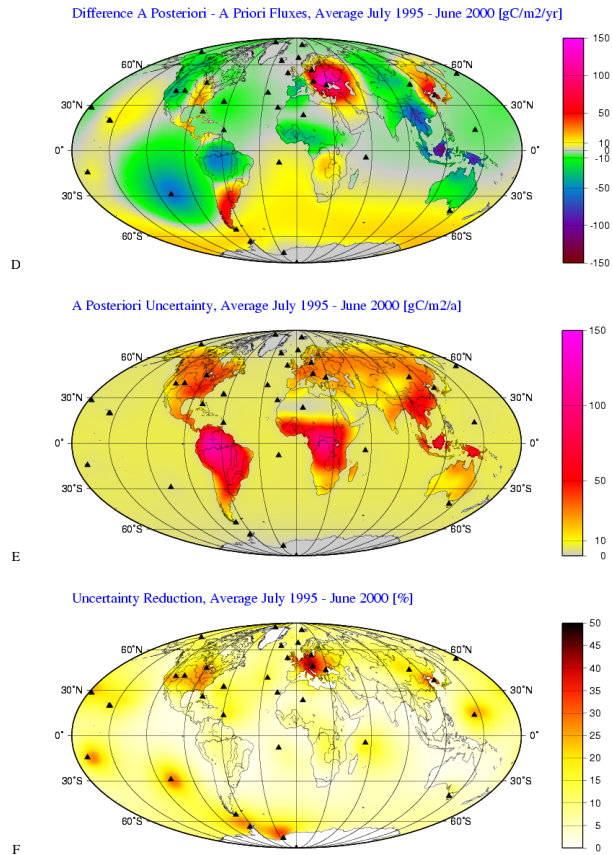


**Fig. 8.** Continued. **(D)** ‘Inversion update’ (deviation of the a-posteriori flux from the a-priori flux). **(E)** A-posteriori uncertainty  $\sigma_{\text{post}}$ . **(F)** Reduction in uncertainty  $(1 - \sigma_{\text{post}}/\sigma_{\text{pri}})$ .

[Title Page](#)
[Abstract](#)
[Introduction](#)
[Conclusions](#)
[References](#)
[Tables](#)
[Figures](#)
[Back](#)
[Close](#)
[Full Screen / Esc](#)
[Print Version](#)
[Interactive Discussion](#)



CO<sub>2</sub> flux history  
1982–2001

C. Rödenbeck et al.

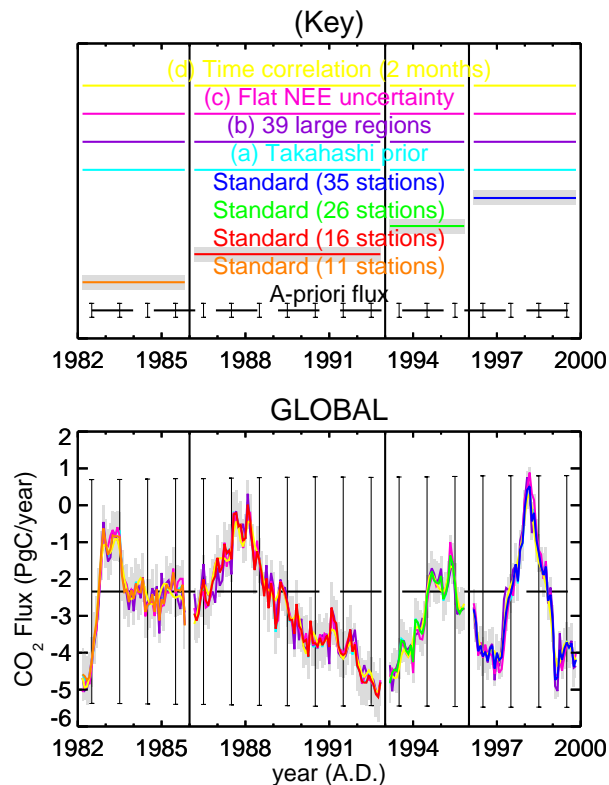


**Fig. 9.** Part I: Measures of uncertainty of the flux estimates: (1) The  $\pm 1\sigma$  intervals of the standard inversion result are depicted as width of the gray shading around the standard flux estimate. They are always smaller than the  $\pm 1\sigma$  intervals of the prior fluxes denoted as error bars. (2) Comparison of the results of the standard inversion with sensitivity set-ups from Table 4. Conventions correspond to Fig. 5. The four sections in time show runs with increasing number of stations (11, 16, 26, or 35, respectively).

Title Page

Abstract

Introduction

Conclusions

References

Tables

Figures

◀

▶

◀

▶

Back

Close

Full Screen / Esc

Print Version

Interactive Discussion

© EGU 2003

**CO<sub>2</sub> flux history  
1982–2001**

C. Rödenbeck et al.

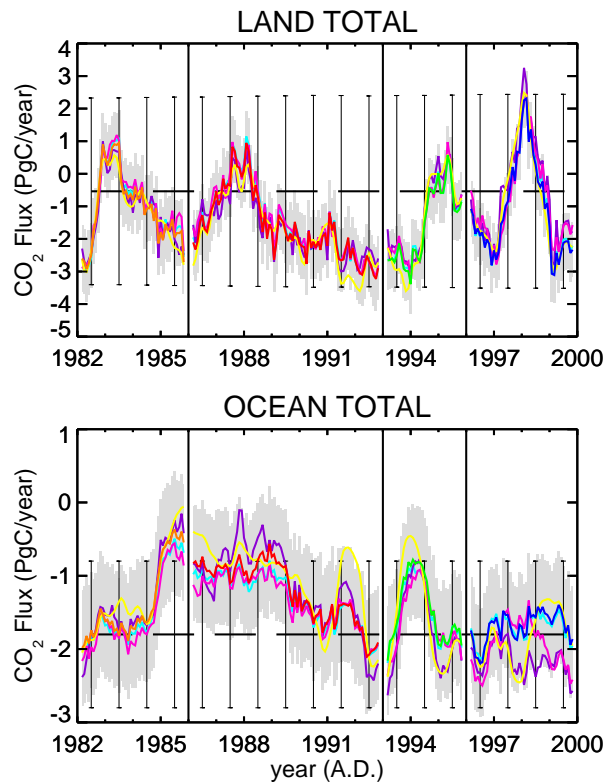


**Fig. 9.** Part II: Measures of uncertainty for the breakup into land-atmosphere and ocean-atmosphere fluxes.

[Title Page](#)[Abstract](#)[Introduction](#)[Conclusions](#)[References](#)[Tables](#)[Figures](#)[◀](#)[▶](#)[◀](#)[▶](#)[Back](#)[Close](#)[Full Screen / Esc](#)[Print Version](#)[Interactive Discussion](#)

© EGU 2003

CO<sub>2</sub> flux history  
1982–2001

C. Rödenbeck et al.

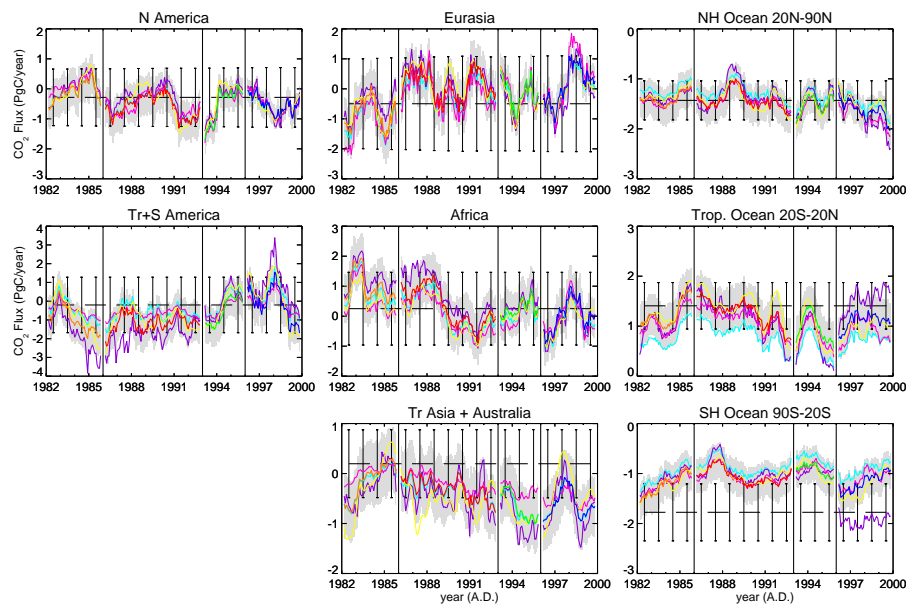


**Fig. 9.** Part III: Measures of uncertainty for the breakup into 5 continental and 3 oceanic regions.

[Title Page](#)[Abstract](#)[Introduction](#)[Conclusions](#)[References](#)[Tables](#)[Figures](#)[◀](#)[▶](#)[◀](#)[▶](#)[Back](#)[Close](#)[Full Screen / Esc](#)[Print Version](#)[Interactive Discussion](#)

© EGU 2003

CO<sub>2</sub> flux history  
1982–2001

C. Rödenbeck et al.

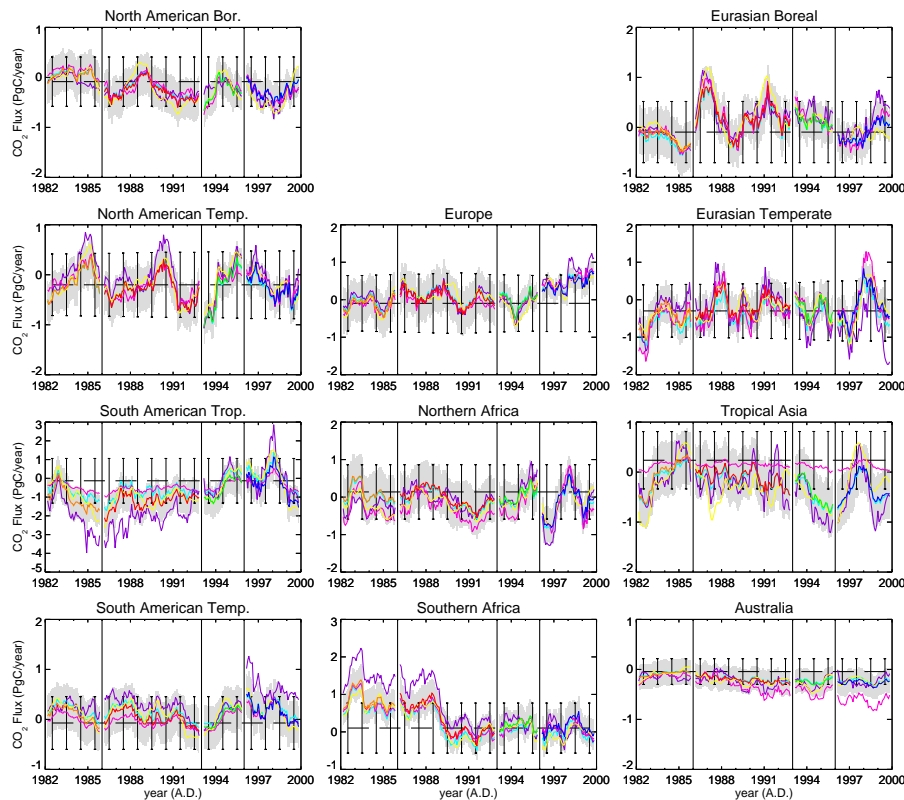


Fig. 9. Part IV: Measures of uncertainty for the 11 land regions of TransCom3.

Title Page	
Abstract	Introduction
Conclusions	References
Tables	Figures
◀	▶
◀	▶
Back	Close
Full Screen / Esc	
Print Version	
Interactive Discussion	

CO<sub>2</sub> flux history  
1982–2001

C. Rödenbeck et al.

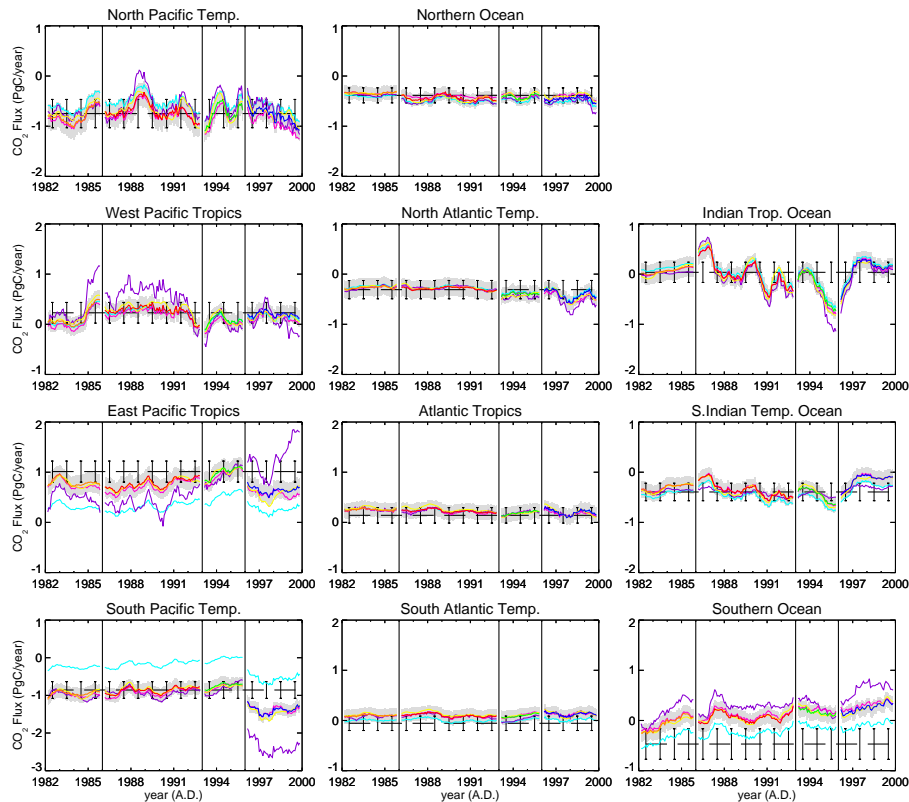


Fig. 9. Part V: Measures of uncertainty for the 11 ocean regions of TransCom3.

Title Page

Abstract Introduction

Conclusions References

Tables Figures

◀ ▶

◀ ▶

Back Close

Full Screen / Esc

Print Version

Interactive Discussion

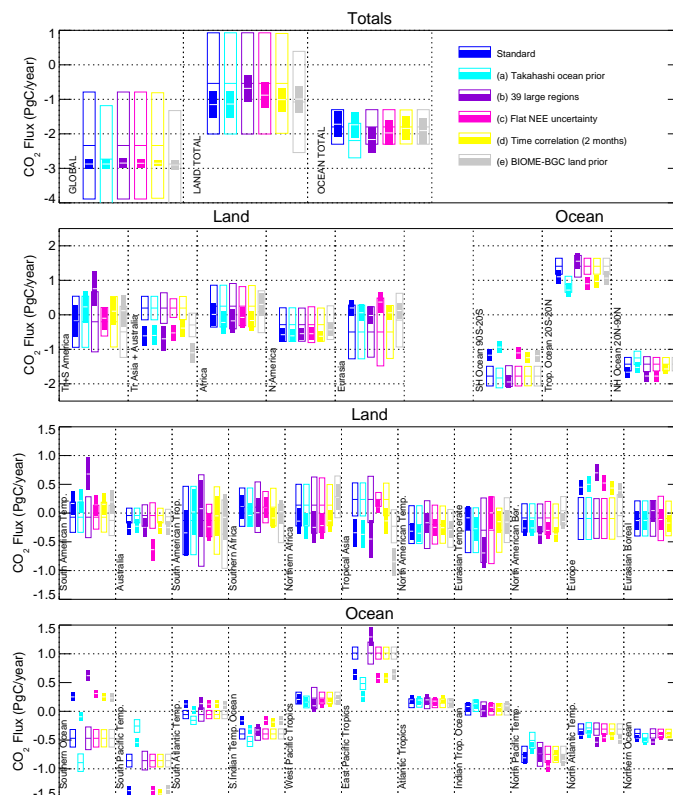


**Fig. 10.** Comparison of the long-term yearly fluxes estimated by different inversion set-ups given in Table 4. Only the results based on 35 stations, averaged over the period 01/1996–12/1999, are shown. The solid coloured bars extend over the a-posteriori  $\pm 1\sigma$  intervals of the averages, with the flux values themselves highlighted as central white lines. The hollow boxes surrounding each bar give the respective a-priori fluxes, which differ both in the best-guess values (at the central horizontal line) and the  $\pm 1\sigma$  intervals (vertical extension of the boxes).

Title Page

Abstract

Introduction

Conclusions

References

Tables

Figures

◀

▶

◀

▶

Back

Close

Full Screen / Esc

Print Version

Interactive Discussion

**CO<sub>2</sub> flux history  
1982–2001**

C. Rödenbeck et al.

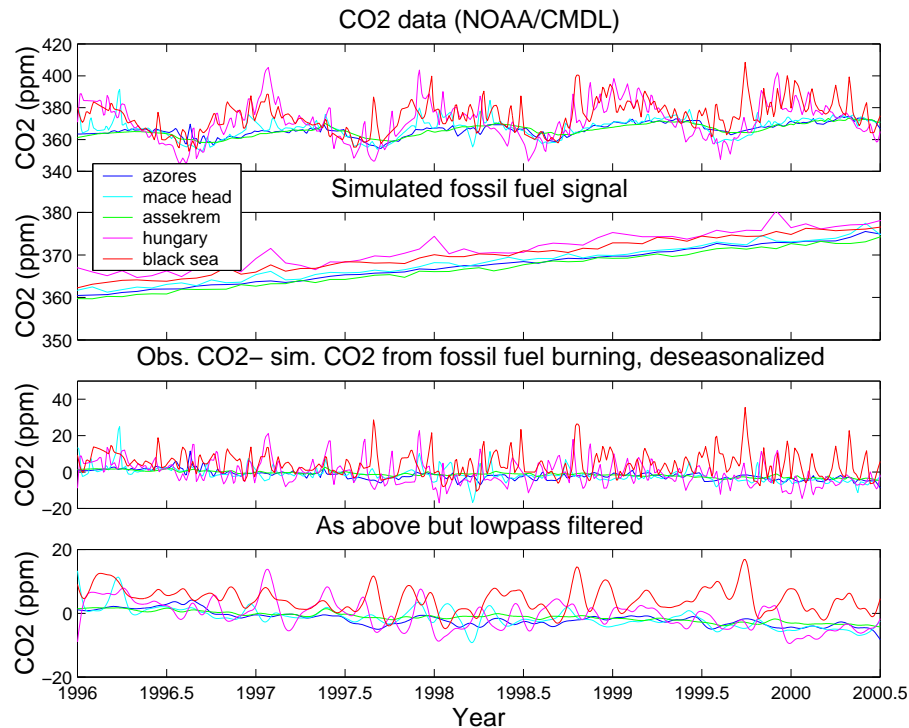


**Fig. 11.** Atmospheric data records at stations located at the continental rim and across Western Europe. Continental rim and background station records are colored in blueish tones and records from continental stations in reddish tones. In the top two panel, the raw data and the simulated fossil fuel signal, respectively, at these stations are displayed. The bottom panels show their differences.

[Title Page](#)[Abstract](#)[Introduction](#)[Conclusions](#)[References](#)[Tables](#)[Figures](#)[◀](#)[▶](#)[◀](#)[▶](#)[Back](#)[Close](#)[Full Screen / Esc](#)[Print Version](#)[Interactive Discussion](#)

© EGU 2003

**CO<sub>2</sub> flux history  
1982–2001**

C. Rödenbeck et al.

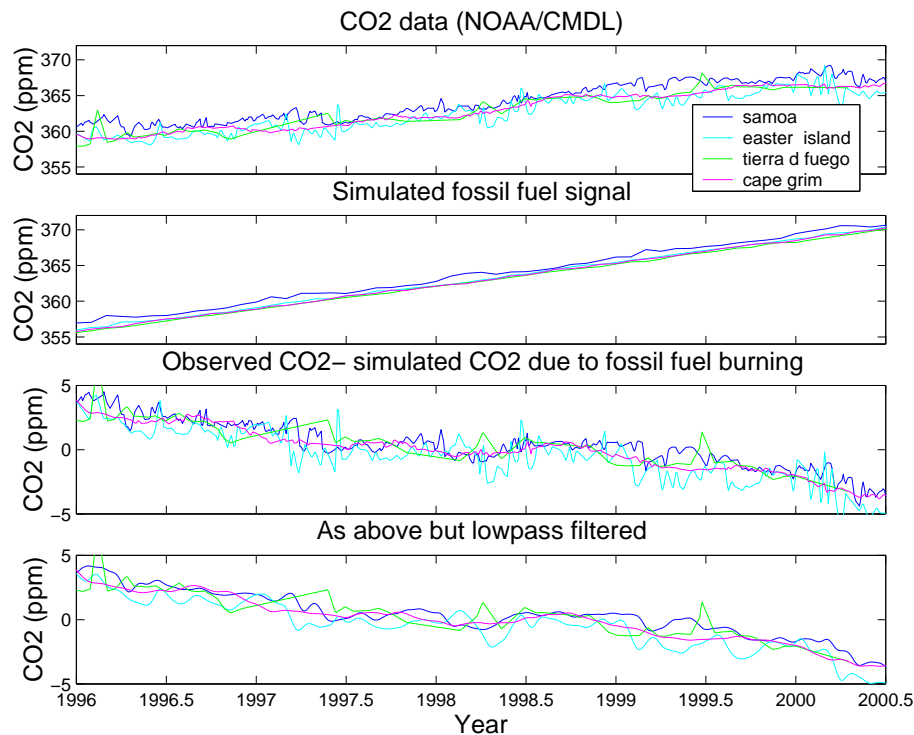


**Fig. 12.** Similar as Fig. 11, for data from stations within or close to the South Pacific temperate region.

[Title Page](#)[Abstract](#)[Introduction](#)[Conclusions](#)[References](#)[Tables](#)[Figures](#)[◀](#)[▶](#)[◀](#)[▶](#)[Back](#)[Close](#)[Full Screen / Esc](#)[Print Version](#)[Interactive Discussion](#)

© EGU 2003



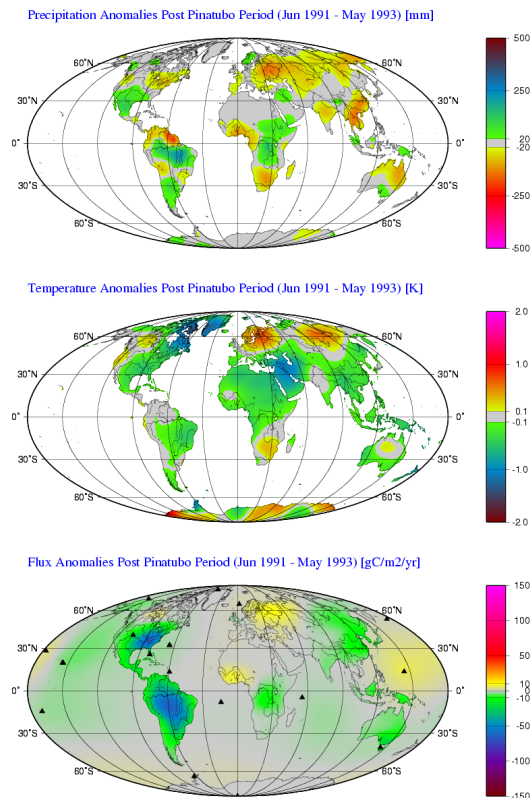


**Fig. 13.** Comparison between climate and CO<sub>2</sub> flux anomalies for the Post-Pinatubo period (06/1991–05/1993). Top: Precipitation anomalies (mm/yr); Middle: Temperature anomalies (K); Bottom: CO<sub>2</sub> flux anomalies (gC/m<sup>2</sup>/yr) estimated with 19 stations. Anomalies are calculated as differences from the reference period 01/1990–12/1999. Precipitation and temperature fields are global analyses by the NCEP weather prediction center.

[Title Page](#)[Abstract](#)[Introduction](#)[Conclusions](#)[References](#)[Tables](#)[Figures](#)[◀](#)[▶](#)[◀](#)[▶](#)[Back](#)[Close](#)[Full Screen / Esc](#)[Print Version](#)[Interactive Discussion](#)

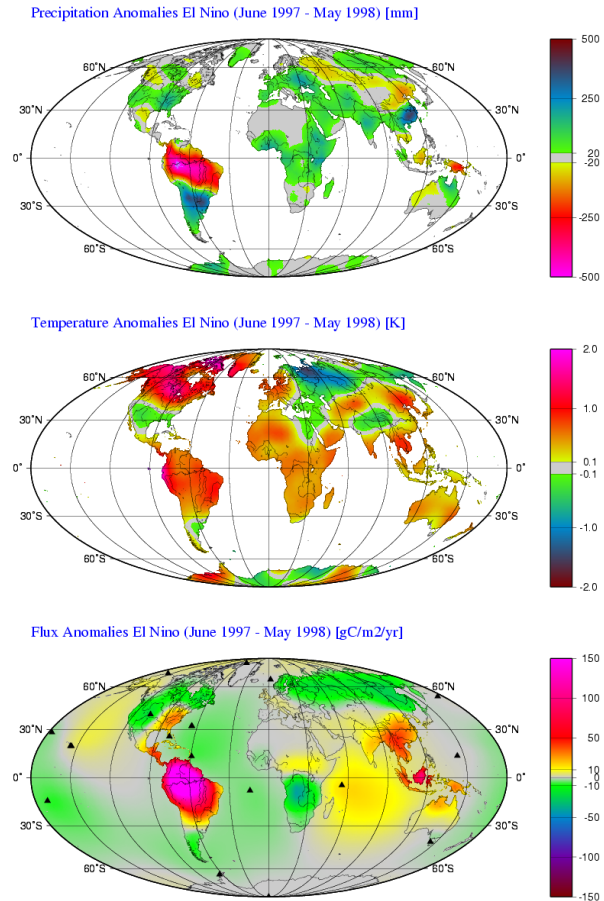


Fig. 14. As Fig. 13 for the 1997/1998 El Niño event (here: period 06/1997–05/1998).

Title Page	
Abstract	Introduction
Conclusions	References
Tables	Figures
◀	▶
◀	▶
Back	Close
Full Screen / Esc	
Print Version	
Interactive Discussion	

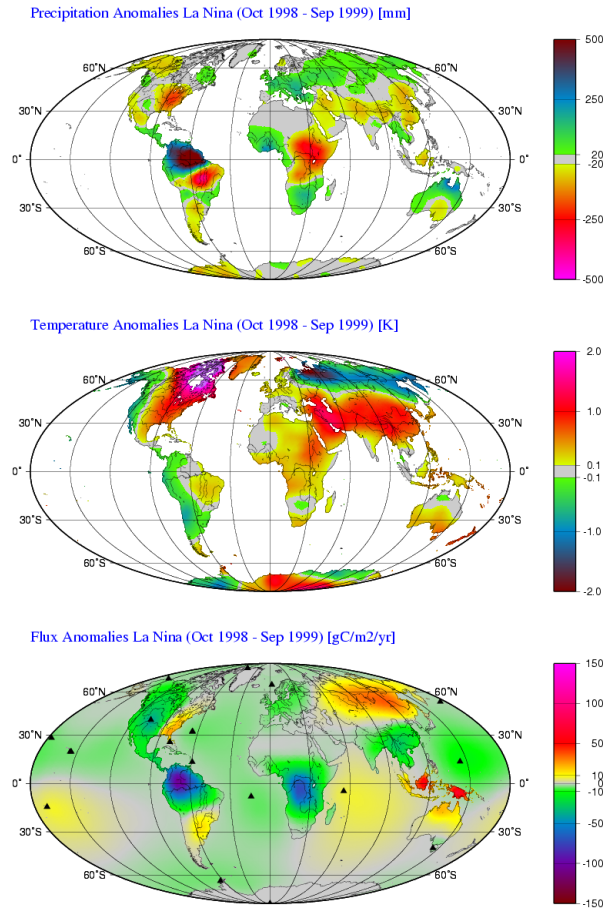
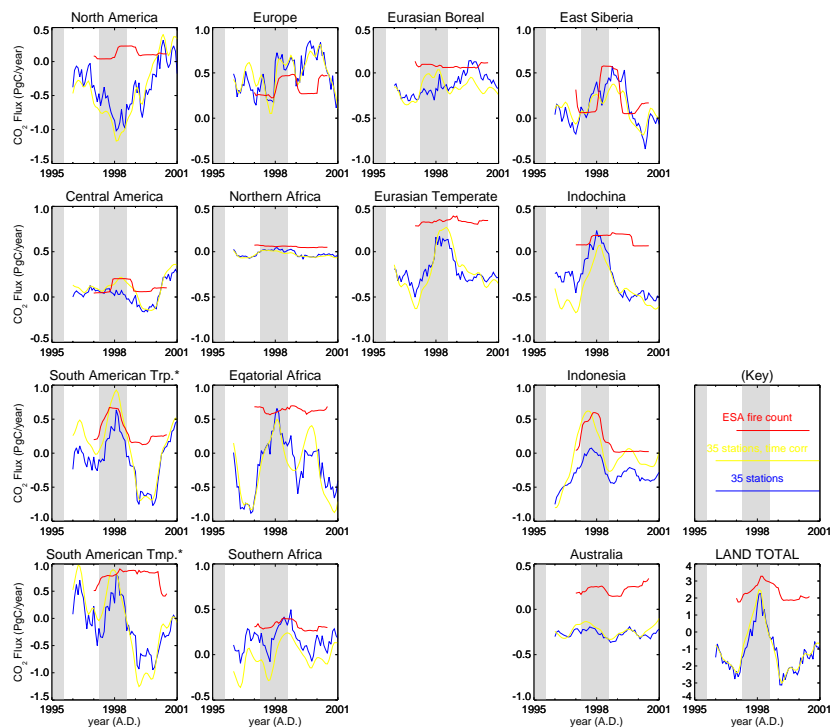


Fig. 15. As Fig. 13 for the 1998/1999 La Niña event (here: period 10/1998–09/1999).

Title Page	
Abstract	Introduction
Conclusions	References
Tables	Figures
◀	▶
◀	▶
Back	Close
Full Screen / Esc	
Print Version	
Interactive Discussion	

CO<sub>2</sub> flux history  
1982–2001

C. Rödenbeck et al.



**Fig. 16.** Comparison of the timing of anomalies in the flux estimates with fire counts measured by the ESA satellite (ATSR World Fire Atlas). Conventions as in Fig. 5. In particular, both fluxes and fire counts are deseasonalized by running 12-months sums, which converts the usually extremely narrow peaks of the fire count (typically one or two months in the fire season of the respective region) into ‘rectangular’ pulses of one year duration centered around the event. The fire counts are scaled by arbitrary factors (independently for each region, but differing not more than 1:5) such that their amplitude be comparable with that of the fluxes. Integration is done over a special set of regions shown in Fig. 17.

Title Page

Abstract

Introduction

Conclusions

References

Tables

Figures

◀

▶

◀

▶

Back

Close

Full Screen / Esc

Print Version

Interactive Discussion

**CO<sub>2</sub> flux history  
1982–2001**

C. Rödenbeck et al.

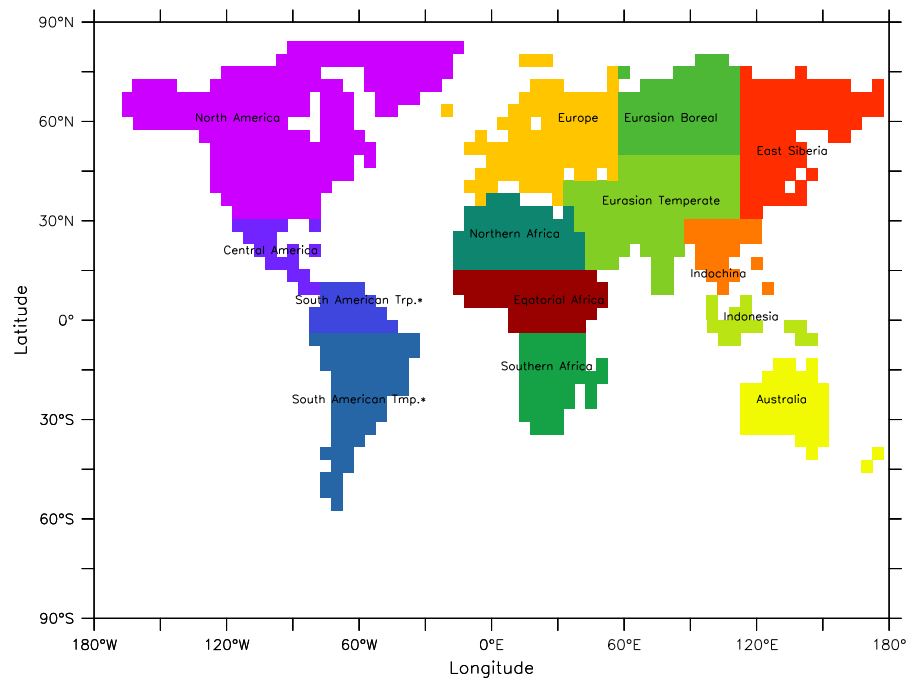


**Fig. 17.** Map of the regions over which the estimated fluxes are integrated to obtain Fig. 16. Conventions as in Fig. 6.

[Title Page](#)[Abstract](#)[Introduction](#)[Conclusions](#)[References](#)[Tables](#)[Figures](#)[◀](#)[▶](#)[◀](#)[▶](#)[Back](#)[Close](#)[Full Screen / Esc](#)[Print Version](#)[Interactive Discussion](#)

© EGU 2003